

Article

Development and Dynamics of Sediment Waves in a Complex Morphological and Tidal Dominant System: Southern Irish Sea

Shauna Creane ^{1,2,3,*}, Mark Coughlan ^{3,4,5}, Michael O'Shea ^{1,2} and Jimmy Murphy ^{1,2}

¹ School of Civil and Environmental Engineering, University College Cork, College Road, T12 K8AF Cork, Ireland

² SFI Research Centre for Energy, Climate and Marine (MaREI), Beaufort Building, Environmental Research Institute, University College Cork, Ringaskiddy, P43 C573 Cork, Ireland

³ Gavin and Doherty Geosolutions, Unit A2, Nutgrove Office Park, Rathfarnham, D14 X627 Dublin, Ireland

⁴ School of Earth Sciences, Science Centre West, University College Dublin, Belfield, D04 N2E5 Dublin, Ireland

⁵ SFI Research Centre for Applied Geosciences (iCRAG), O'Brien Centre for Science East, University College Dublin, D04 N2E5 Dublin, Ireland

* Correspondence: shauna.creane@ucc.ie

Abstract: With the recent push for a transition towards a climate-resilient economy, the demand on marine resources is accelerating. For many economic exploits, a comprehensive understanding of environmental parameters underpinning seabed morphodynamics in tidally-dominated shelf seas, and the relationship between local and regional scale sediment transport regimes as an entire system, is imperative. In this paper, high-resolution, time-lapse bathymetry datasets, hydrodynamic numerical modelling outputs and various theoretical parameters are used to describe the morphological characteristics of sediment waves and their spatio-temporal evolution in a hydrodynamically and morphodynamically complex region of the Irish Sea. Analysis reveals sediment waves in a range of sizes (height = 0.1 to 25.7 m, and wavelength = 17 to 983 m), occurring in water depths of 8.2 to 83 mLAT, and migrating at a rate of 1.1 to 79 m/yr. Combined with numerical modelling outputs, a strong divergence of sediment transport pathways from the previously understood predominantly southward flow in the south Irish Sea is revealed, both at offshore sand banks and independent sediment wave assemblages. This evidence supports the presence of a semi-closed circulatory hydrodynamic and sediment transport system at Arklow Bank (an open-shelf linear sand bank). Contrastingly, the Lucifer–Blackwater Bank complex and associated sediment waves are heavily influenced by the interaction between a dominant southward flow and a residual headland eddy, which also exerts a strong influence on the adjacent banner bank. Furthermore, a new sediment transfer system is defined for offshore independent sediment wave assemblages, whereby each sediment wave field is supported by circulatory residual current cells originating from offshore sand banks. These new data and results improve knowledge of seabed morphodynamics in tidally-dominated shelf seas, which has direct implications for offshore renewable developments and long-term marine spatial planning.

Keywords: sediment waves; sand banks; modelling; Irish Sea; sediment transport; seabed morphodynamics

Citation: Creane, S.; Coughlan, M.; O'Shea, M.; Murphy, J. Development and Dynamics of Sediment Waves in a Complex Morphological and Tidal Dominant System: Southern Irish Sea. *Geosciences* **2022**, *12*, 431. <https://doi.org/10.3390/geosciences12120431>

Academic Editors: Katrien Van Landeghem and Jesus Martinez-Frias

Received: 5 October 2022

Accepted: 17 November 2022

Published: 23 November 2022

Publisher's Note: MDPI stays neutral with regard to jurisdictional claims in published maps and institutional affiliations.



Copyright: © 2022 by the authors. Licensee MDPI, Basel, Switzerland. This article is an open access article distributed under the terms and conditions of the Creative Commons Attribution (CC BY) license (<https://creativecommons.org/licenses/by/4.0/>).

1. Introduction

1.1. Seabed Morphodynamics

A comprehensive understanding of sediment dispersal and seabed morphodynamic processes on tidally-dominated shelf seas [1–8] is paramount for a wide range of economic exploits including: the location and evolution of benthic habitats directly impacting fisheries [9,10], the need to monitor the volume of marine aggregates [11], the impact of

coastal flooding and erosion protection measures [12–14], the prevention of free-spanning and burial of offshore infrastructure such as pipelines and cables [15,16], and reducing the risk of scour formation around offshore wind turbine foundations inherently leading to critical infrastructural instability [17,18]. With the recent push for a transition towards a climate-resilient economy, both at national and regional levels, ambitious 2030 offshore wind capacity targets have been set at 7 GW and 50 GW for the Republic of Ireland and UK respectively [19–21]. This heightened demand on marine resources calls for efficient marine spatial planning. With predicted future sea level rise potentially altering the spatial distribution of tidal constituents across tidally-dominated continental shelves [22,23], the dependent sediment transport regime subsequently could be altered [5]. Consequently, a fundamental knowledge of environmental parameters underpinning seabed mobility and evolution over time, and the relationship between local and regional scale sediment transport regimes as an entire system, is imperative. Investigation into the present-day interaction between these processes will ultimately facilitate the composition and implementation of more robust long-term marine spatial planning. The formation of submarine morphological features is dependent upon the interaction between regional sedimentary systems and local hydrodynamic conditions. Two main categories of submarine geological features have been described by Stow, et al., [24]; (i) linear bedforms that develop elongated, parallel or oblique to flow direction, and (ii) transverse bedforms that are relatively regular undulating features occurring perpendicular to flow. Plan- and cross-sectional analysis of sediment banks (linear bedforms) and sediment waves (transverse bedforms) are used to define bed load transport pathways in tidally-dominated shelf seas and are very important to understanding seabed evolution over time.

1.1.1. Sediment Banks and Sediment Waves as Indicators of Sediment Transport Dynamics

Sediment banks are widespread across the European continental shelf, having formed under a variety of conditions [5,25]. In the Irish Sea and North Sea, sand banks are potential sites for present and future offshore wind farm developments, for example, Arklow Bank and Scroby Sands respectively. Where sand bank geometry can indicate regional scale net tidal flow and net sediment transport pathways [26–28], sediment waves associated with sand banks indicate localised sediment transport regimes. As sediment wave migration rates (migrating up to tens of metres per year [29,30]) are one order of magnitude higher than sand banks, they pose significant threat to the offshore wind industry [31]. For example, exposure or burial of submarine cables [15], and interaction with turbine foundations and protection structures, inherently lead to infrastructural instability [18]. Therefore, the temporal and spatial evolution of bedform morphology, and the localised transport pathways, are of critical importance to offshore industries. The impact of migrating sediment waves and other bedforms on manmade seabed structures remains understudied. Using a combination of repeat bathymetric survey data and hydrodynamic modelling, Couldrey, et al., [32] analysed the morphological evolution of a barchan dune as it passed a monopile foundation at an average migration rate of 25 m/yr to assess its impact on sedimentary processes at the base of the structure. Overall, despite changes in seabed morphology at the site including scouring processes, they found that the dune's presence did not impact significantly on the stability of the wind turbine, nor its operational performance. However, this represents a single study of an isolated sediment wave (a barchan dune) passing a structure, whereas in areas such as the Irish Sea, multiple individual sediment waves of varying heights may pass and interact with a particular feature.

The oblique alignment of a linear sand bank axis to the net tidal flow generates a flood and ebb dominance on either flank of the bank [33]. On active sand banks this is ultimately reflected in sediment wave asymmetry, where sediment lee slopes face in opposite directions on either side of the bank [25,34]. Identification of symmetrical sediment waves at the end of sand banks, in conjunction with the progressive orientation change of the sediment wave crests, from bank base to bank crest, towards almost parallel alignment with the bank

crest, led to the conclusion that circulation around and over the bank is what maintains the sand bank [35,36]. Leenders, et al., [37] supports this theory by successfully modelling the migration directions of sediment waves up and over sand banks in the North Sea, reasonably matching observational studies. Horrillo-Caraballo, et al., [38] further supports the presence of this circulatory flow pattern by identifying residual gyre patterns around sand banks in the Irish Sea by plotting the vorticity of the residual flow. Nevertheless, Johnson, et al., [28] suggests circulation around sand banks does not necessarily suggest a closed circulatory hydrodynamic and sediment transport system. Creane, et al., [5] supports this concept by using numerically modelled residual tidal current and bed shear stress to identify two residual transport pathways capable of providing sediment flux into Arklow Bank’s (Irish Sea) (Figure 1) localised circulatory system. However, ground-truthing evidence such as analysis of repeat bathymetric datasets to quantify bedform spatial and temporal evolution, and net transport pathways, are absent in the area.

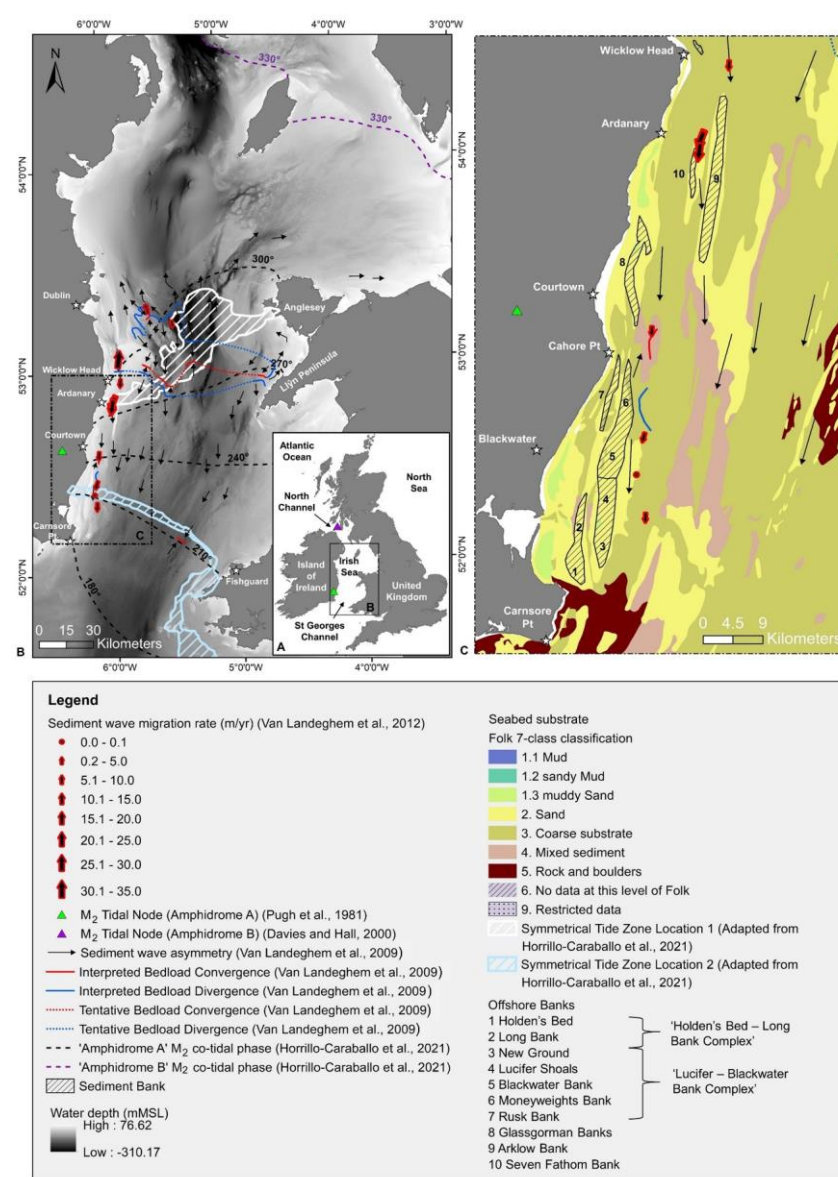


Figure 1. Maps showing pre-existing knowledge of Irish Sea sediment transport. (A) Location of the Irish Sea on the north-western European continental shelf. (B) Irish Sea hydrodynamic and sediment transport characteristics. The location of the bedform derived bed load parting zone, defined by Van Landeghem, et al., [39], characterised by one main sediment transport convergence zone and two divergent zones, is indicated. Bathymetry source: EMODnet Bathymetry Consortium [40]. (C) Study area displaying sediment distribution and main offshore sediment banks. Seabed substrate source:

European Marine Observation Data Network (EMODnet) Seabed Habitats initiative (<http://www.emodnet-seabedhabitats.eu/> [Accessed: 25 June 2021]) [41].

Under uni-directional flow, sediment wave migration is found to be in direction of asymmetry. This is found to be mostly true under bi-directional flow. This assumption has been used to estimate migration rates [29,42,43], and to depict sediment transport pathways on a regional scale across tidally dominated shelf seas [5,26,27,39,44]. Analysis of high resolution time-lapse bathymetric data challenges this assumption through observations of counter-current migration and reversals in sediment wave asymmetry [30]. Damen, et al., [45] found a negative correlation between sediment wave asymmetry and residual transport direction, further falsifying this theory. Thus, this strongly suggests that ground-truthing datasets are necessary to aid the quantification of spatial and temporal evolution in tidally-dominated seas. Furthermore, the comparison of repeat multibeam echo sounder datasets against environmental and theoretical-based indicators may further resolve gaps in academic knowledge.

1.1.2. Controlling Factors on Sediment Wave Growth

On tidally-dominated shelves, sediment waves also occur independently of larger bedforms (i.e., sand banks, marine channels or troughs), existing in isolation or in assemblages, in two- or three-dimensional form [46]. The basic description of sediment wave geomorphology is predominately based on the sediment wave height (H) to wavelength (L) ratio whereby local datasets are commonly compared to their positive exponential relationship ($H_{mean} = 0.0677L^{0.8098}$, $r = 0.98$, $n = 1491$) derived from the global dataset established by Flemming [47] (Table 1). This relationship was previously thought to represent an equilibrium state of active sediment waves, however, Flemming [48] re-defined it to represent an approximate generalised global trend whereby departures from the trend indicate the influence of local process-response mechanisms characteristic of in situ environments [4,39,45,49]. Flemming [48] further suggests an upper limit to sand wave growth ($H_{max} = 0.16L^{0.84}$) depending on water depth, flow velocity, and grain size. To date, numerous research results (e.g., Blondeauz and Vittori [50] and van Santen, et al., [51]) show that quantifying the sensitivity of sediment waves to individual local environmental parameters has proven to be a difficult task.

Yalin [52] suggests a relationship between sand wave height and water depth, however this association has been highly debated [48,53,54]. Where Van Der Veen, et al., [53] found a good correlation between the occurrence of sediment waves in the North Sea and grain size, water depth and flow velocity, many research studies show poor correlations with sand wave dimensions and water depth [55,56]. Flemming [48] suggests water depth does not play an important role on sediment wave vertical growth in deeper waters, instead grain size is the dominant controlling factor. Sediment availability is also a suggested limiting factor [48]. Contrastingly, Zhou, et al., [4] found that sand waves tend to grow higher and shorter with decreasing water depths, and lower and longer with increasing water depths. This is attributed to a higher growth rate in wavelength in comparison to wave height due to the amalgamation process, leading to a more subdued bedform. Nonetheless Zhou, et al., [4] does not include grain size, current velocity, and other influencing environmental parameters in their analysis, therefore external factors may be influencing this relationship. For instance, a moderate to good correlation between sand wave growth and water depth may signify a relationship with environmental parameters associated with water depth variations, i.e., current velocity acceleration/deceleration, rather than water depth itself acting as the controlling factor. A modelling study by Blondeaux and Vittori [50] revealed a correlation between increasing sediment wave wavelengths and increasing water depths and/or decreasing tidal current velocities. Similarly, van Santen, et al., [51] found that an increase in depth-averaged maximum tidal current velocity correlated very well with decreasing wavelength under both field and

modelled datasets. However, the same study could not detect a dependence of wavelength on water depth or grain size in field data as indicated by theoretical predictions [51]. Consequently, in the natural environment, a complex, dynamic coupling of a variety of environmental factors most likely impact sediment wave growth, therefore process-based indicators may be more suited to this investigation.

Process-based indicators (e.g., Rouse numbers that indicate the mode of sediment transport) have proven useful at quantifying large scale sediment wave dynamics. Hulscher [57] shows that under linear stability analysis, sediment wave growth is due to a residual vertical circulation by the tidal flow. Over an ebb and flood tidal cycle, the upslope flow is dominant over the downslope flow, resulting in a convergence of sediment transport pathways at the bedform crest, triggering bedform growth. Damen, et al., [45] supports this existing theory suggesting that the mode of sediment transport is an important sediment wave growth damping mechanism. Specifically, on the Dutch Continental Shelf, Damen, et al., [45] found a strong positive relationship between the occurrence of sand wave fields and bed load transport dominance, and a negative relationship with increasing suspended transport dominance. An increase in the ratio of suspended load transport to bedload transport represents an enhanced entrainment of finer grains into the water column, thus inhibiting the growth of sediment wave heights [45,58–60]. Consequently, as critical suspension velocity is higher for coarser grains, sediment wave heights positively correlate with increasing grain sizes [4,45,56]. Positive correlations between grain sizes and Rouse numbers with sediment wave heights suggests the relative dominance of bed load transport over suspended load affects bedform growth [45,60]. The mode of sediment transport is considered an important damping mechanism by many studies [45,48,61]. Consequently, it is evident that the dynamic coupling of multiple environmental parameters and processes must be considered when investigating bedform growth and development

Furthermore, in addition to tidal current, sediment supply is a major control on whether independent sediment wave fields remain active or become moribund. A lack of studies on these mechanisms in tidally-dominated shelf seas is evident. Investigation into these mechanisms is key to understanding the sediment transport regime as a whole system.

Table 1. Geometrical relationships of sediment waves from previous studies.

Reference	Power Regression Equation	Correlation Coefficient (r)	Environment
Van Landeghem, et al., [56]	$H_{mean} = 0.0692L^{0.802}$	0.85	Irish Sea in water depths of 20 m to 179 m
Flemming [47]	$H_{mean} = 0.0677L^{0.8089}$		Global dataset
Flemming [47]	$H_{max} = 0.16L^{0.84}$		Global dataset
Zhou, et al., [4]	$H_{mean} = 0.0625L^{0.8125}$	0.94	Giant sand waves on Taiwan Banks (full dataset)
Zhou, et al., [4]	$H_{mean} = 0.052L^{0.86}$	0.96	Giant sand waves on Taiwan Banks (symmetrical to symmetrical–asymmetrical sand waves)
Zhou, et al., [4]	$H_{mean} = 0.0005L$	0.1	Giant sand waves on Taiwan Banks (double-crested sand waves)
Zhou, et al., [4]	$H_{mean} = 0.0018L$	0.2	Giant sand waves on Taiwan Banks (asymmetrical sand waves)
Francken, et al., [62]	$H_{mean} = 0.0321L^{0.918}$	0.9	Scheldt Estuary

Dalrymple, et al., [63]	$H_{mean} = 0.0635L^{0.733}$	0.791	Bay of Fundy, Canada
-------------------------	------------------------------	-------	----------------------

1.2. Study Aims

The complex hydrodynamic and morphodynamic regime in the southern Irish Sea provides a unique opportunity to analyse both independent and sand-bank-associated sediment wave fields separately in their localised environments, as well as the relationship between sand banks and associated sediment wave assemblages, and independent offshore assemblages. Therefore, this study will address the following hypotheses:

1. Mobile independent sediment wave assemblages and sand-bank-associated sediment wave assemblages are supported by independent sediment transport systems.
2. Linear sediment banks do not exhibit a closed circulatory transport system yet reveal a semi-closed circulatory transport regime.

To investigate these hypotheses, this study aims to:

- (a) Describe the morphological characteristics of sediment waves and their spatio-temporal evolution in a tidally dominated, shallow shelf setting in NW Europe;
- (b) Estimate sediment wave migration rate and infer sediment transport flux, relating the data to the wider sediment transport and hydrodynamic regime of the region;
- (c) Investigate whether there is a relationship between sand banks and independent sediment wave assemblages.

2. Regional Setting

Located on the western European continental shelf, the Irish Sea is a semi-enclosed body of water connected to the Atlantic Ocean via two openings: the North Channel and St Georges Channel (Figure 1A). The focus of this study is the south-western section within 30 km from the east coast of Ireland, which incorporates a complex degenerate amphidrome [5] (Figure 1C). This area exhibits intricate seabed morphologies and a complex sediment transport regime. The Irish Sea is driven by tidal forcing, wind shear stress and baroclinic flow, which in turn are major drivers of seabed mobility and sediment distribution. Tide-induced bed shear stress is shown to be the dominant physical process driving seabed mobility in the south-western Irish Sea, with wave-action enhancing mobility in relatively shallow areas such as the southern banks (e.g., Lucifer–Blackwater Bank complex) [64]. Due to intricate basin geometry, a convoluted tidal regime exists. Tidal vectors in the Irish Sea are dominated by M_2 and S_2 constituents, whereby M_2 dominates. The tidal wave propagates into the Irish Sea through St Georges Channel and is continuously both deflected to the right by Coriolis forcing, and reflected northwards by intricate bathymetry and coastline topography. Ultimately, this generates an anticlockwise rotary wave around a degenerate amphidromic point (Amphidrome A) pinpointed on the east coast of Ireland at Courtown (Figure 1). This anticlockwise rotation produces high tidal ranges on the east coastline of the Irish Sea and near net zero tidal ranges at this degenerate amphidrome on the west coastline. The flood tidal wave entering through the North Channel rotates around a similar yet pure (offshore tidal node) anticlockwise amphidromic system (Amphidrome B) (Figure 1). These two flooding tidal waves intersect at an angle along a transect approximately from Ardanary to Anglesey, generating a symmetrical tidal system [38] and a bed load parting zone [26–28,39] (Figure 1). The shape and location of this bed load parting zone is further controlled by the change in tidal character at abrupt bathymetric changes, headlands and intricate coastline topography, and large-scale constrictions [5].

This bed load parting zone marks the ‘head’ of regional scale divergent bedload transport paths. These are supported by divergent residual flow and bed shear stress vectors [5]. These residual flows support previously bedform-derived bedload transport pathways [26,27,30,39] in the south-western Irish Sea to a certain point [5]. However, this region is highly dynamic, containing many morphodynamic bedforms, and many large

morphological features known to diverge from regional scale patterns (sand bank systems and sediment wave assemblages) have yet to be analysed in detail using repeat time-lapse geophysical datasets.

Sediment distribution in the Irish Sea has been characterised by multiple studies [27,39,65–69]. The south-western Irish Sea is dominated by coarse non-cohesive sands and gravels (clastic sediments) [68] (Figure 1C). In regions where sediment supply is limited, the upper mobile layer of Holocene sediments may be limited or absent, resulting in the exposure of the Pleistocene glacial till, or rarely exposed bedrock. In areas of high sediment supply, a transition from coarse-lag gravels and gravelly sands into thick mobile sand sheets (up to 40 m thick) are evident [5,9]. Both active and moribund sediment waves (some reaching 36 m high) characterise the south-western Irish Sea [56], with migration rates reaching a maximum average of 32 m/yr [30]. Additionally, a series of coast-parallel bedforms are located in approximately 20–40 m water depth rising to only a couple of metres below sea level (Figure 1). A variety of studies characterise these sandbanks as being ‘active’, displaying a highly mobile top layer of surficial sediments [66,70,71], however, there is a significant paucity of high spatial and temporal resolution sand bank morphodynamic and seabed stability studies under present day hydrodynamics. These complex bathymetries diverge from the net southward residual bedload transport pathway and increase the complexity of localised sediment transport pathways in the region, yet the extent of this divergence and the driving factors are poorly understood.

3. Materials and Methods

3.1. Multibeam Echo Sounder Data Acquisition and Processing

Since 2006, high resolution swath bathymetry data has been collected across the Irish sector of the Irish Sea by the Republic of Ireland’s INFOMAR (Integrated Mapping for the Sustainable Development of Ireland’s Marine Resource) programme, a joint venture between the Geological Survey of Ireland and the Marine Institute funded by the Department of the Environment, Climate and Communications (DECC). These acoustic datasets were collected either using (i) the hull-mounted Kongsberg Simrad EM2040 and EM3002 multibeam echo sounder (MBES) models via the RV *Celtic Voyager* and RV *Keary*, or (ii) the Teledyne Reson Seabat T20-P MBES model which is mounted to a retractable A-frame onboard the RV *Lir*. The vessel, and thus the instrument, used predominately depended on water depth and vessel availability.

All relevant INFOMAR datasets were collated at the highest available spatial resolution (2 m or 5 m) and integrated into a mosaic raster dataset using ArcGIS v10.8 (Figure 2). This dataset was used as baseline bathymetry for a preliminary interpretation framework that aimed to identify seabed features and to compute morpho-metric measurements of transverse marine bedforms. Preliminary seabed characterisation and mapping was carried out using elements of the ArcGIS’ Benthic Terrain Modeller [72], and geomorphon analysis [73] within GRASS GIS. Based on these interpretations, 12 sub-areas were identified for further geophysical surveying and geological sampling (Figure 2).

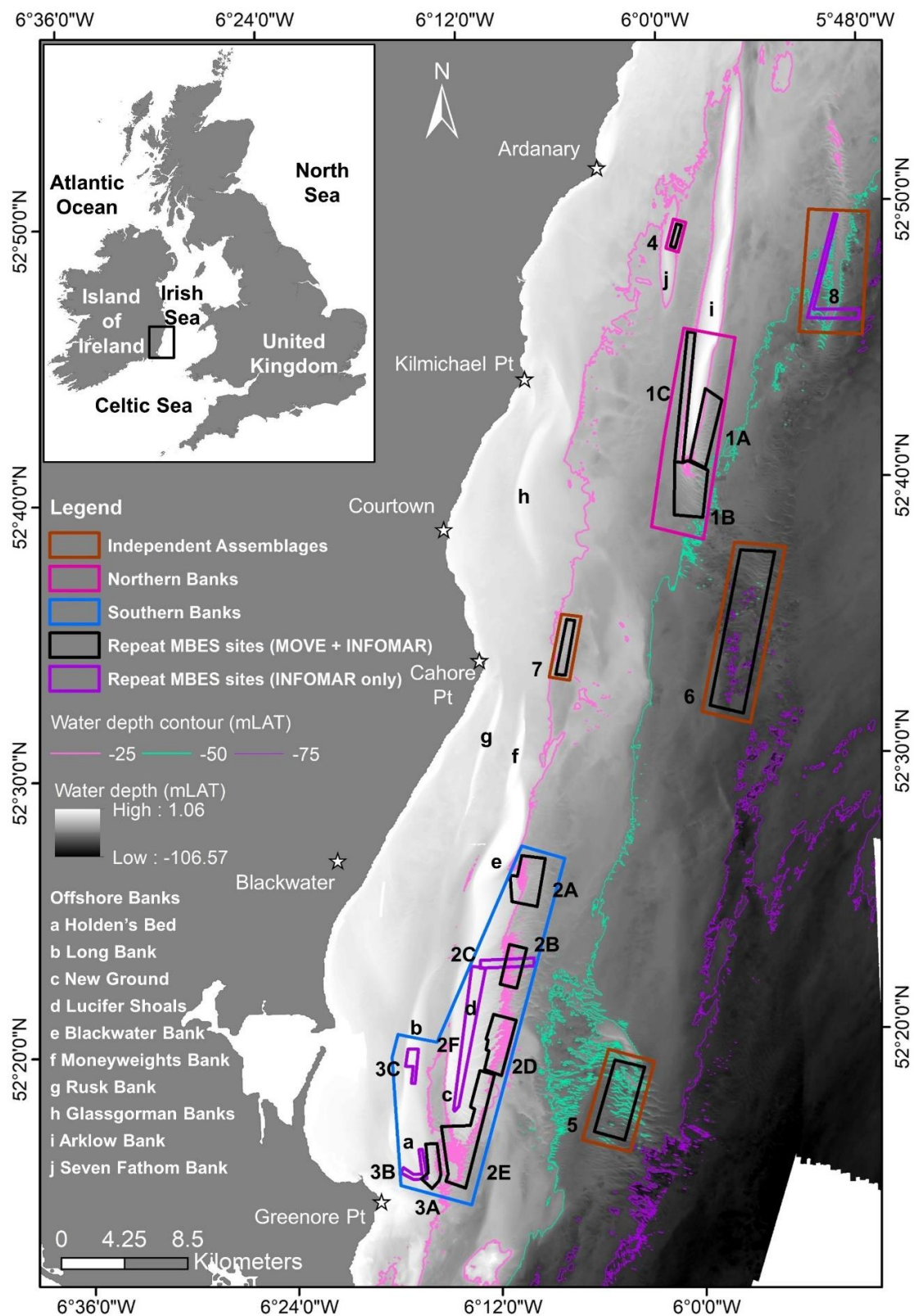


Figure 2. Location of multi-beam echo sounder (MBES) bathymetry datasets analysed in this study. Available datasets at each site are presented in Table 2. Sites are grouped into three environments for sediment wave analysis: Independent Assemblages, Northern Banks and Southern Banks, which are indicated by blue, pink, and green polygons respectively. Bathymetry source: composite map produced from INFOMAR datasets (<https://www.infomar.ie/data> [Accessed: 10 June 2021]) (see Section 3.1).

Additional repeat MBES data was acquired on three targeted surveys in 2020 and 2021 onboard the *RV Celtic Voyager* (Table 2).

The Mobility of Sand Waves and Sediment Banks (MOVE) offshore survey campaigns involved targeted MBES work over the 12 identified sites, onboard the *RV Celtic Voyager*. A Kongsberg dual head EM2040 was used operating at 300 kHz and a beam angle of 69° to 75° on both port and starboard side, depending on water depth. Accurate positioning was provided by an Integrated GNSS/L-Band receiver CNAV 3050 (horizontal/vertical accuracies of +/-5 cm/10 cm). Data was logged onboard using the Kongsberg’s Seafloor Information System (SIS) v. 3.83 acquisition software. A Valeport Sound Velocity Profiler (SVP) Mini instrument was used to acquire SVP profiles, which were imported into SIS and fed directly into the echosounder. Using Qimera v2.3.1, all MBES datasets were processed to remove erroneous pings and correct for tidal and water displacement offsets. MBES-derived bathymetry datasets were reduced to Lowest Astronomical Tide (LAT) using a Vertical Offshore Reference Frame (VORF). Quality control was performed using crosslines where available. Datasets were georeferenced using GCS WGS 1984 geographic co-ordinate system and output in raster format at 1 m spatial resolution.

Table 2. Details of MBES bathymetry datasets used in this study. Location of each site is presented in Figure 2.

INFOMAR Bathymetry Datasets							Mobility of Sand Waves and Sediment Banks (MOVE) Bathymetry Datasets		
Year Collected	2009	2011	2012	2015	2016	2017	2020 (Sep)	2020 (Oct)	2021 (Mar)
Offshore Survey Codes	CV09_03	KRY11_02 CV11_03	CV12_02 CV12_01	KRY15_03	KRY16_03 GEO16_03 KRY16_02	LIR17_01 KRY17_02	CV20010	CV20035	CV21035
Spatial resolution (m)	2	2 5	2 5	2	2	2	1	1	1
Sites	1A	√	√		√		√		√
	1B		√	√		√	√		
	1C		√	√		√	√		√
	2A			√			√		√
	2B	√		√			√	√	√
	2C	√		√					
	2D	√					√		√
	2E	√					√		√
	2F				√		√		
	3A	√					√		
	3B	√	√						
	3C	√	√				√		
4		√					√	√	
5			√				√	√	
6			√				√		

7		√	√	√
8	√	√		

3.2. Sediment Wave Analysis

Areas of time-lapse bathymetric data were identified for further analysis. These included datasets from the MOVE offshore survey campaigns, and areas of relatively small overlap between the INFOMAR datasets. Eight main areas, comprising 17 sub-areas in total, were identified. The location and available datasets for each site are presented in Figure 2 and Table 2.

3.2.1. Sediment Wave Geometric Characteristics

Sediment wave characterisation is a key component in classifying the geomorphology of a sediment wave and in inferring bedform dynamics over time. Previously, the delineation of sediment wave crests has largely relied on manual digitisation based on MBES and MBES-derived datasets (e.g., slope) [30]. Similarly, the derivation of bedform dimensions has mainly depended on cross-sectional profiles derived from these MBES datasets [56]. More automated methods have included geomorphometry [73], object-based image analysis [74], the second derivative [75], curvature [76], and zero-crossing analysis [77]. The application of Fourier analysis has also proven successful in sediment wave characterisation [78]. Following a review of applications, it was found the approach of Wang, et al., [78] was the most appropriate for sediment wave characterisation due to its ease of use and accuracy of results.

The automated MATLAB-based method for analysing bedform geometry parameters was applied to the baseline (earliest) bathymetry dataset at each site. This tool combines 2D Fourier analysis, wavelet transform, zero-crossing analysis and a variety of filters. Sediment wave dimensions defined by this tool and adopted by this study are given in Figure 3, where sediment wave asymmetry (A) is given as

$$A = \frac{L_1 - L_2}{L} \quad (1)$$

and water depth (d) of a sediment wave is expressed as

$$d = d(cr) + H \quad (2)$$

where $d(cr)$ is the water depth of the sediment wave crest and H is sediment wave height. Sediment wave parameters were used to classify bedforms at each site according to the sizing system adopted by Van Landeghem, et al., [56] and Evans, et al., [79], originally adapted from Ashley [46] and Berne, et al., [80] (Table 3). Similar to Van Landeghem, et al., [56], the term 'sediment wave' is used in this study to describe large flow-transverse bedforms and the terms 'sand wave' or 'gravel wave' are used when sediment composition could be determined.

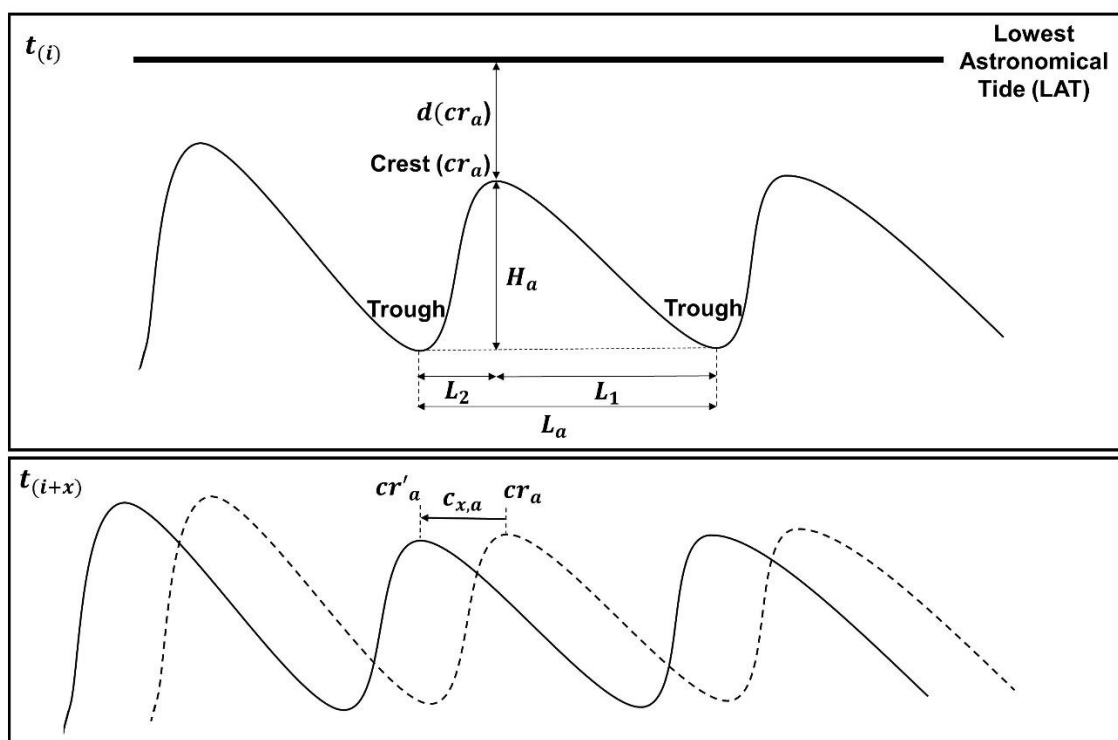


Figure 3. Illustration representing sediment wave (SW) characteristics used in this study. For SW “a”, the Figure denotes $cr = a$; $d(cr)$ = water depth of SW crest; H = SW height; L = SW wavelength (and length components L_1 and L_2); $t_{(i)}$ = time of first bathymetric survey over SW field; $c_{(x)}$ = displacement of SW crest over time interval x ; cr' = position of displaced SW crest over time interval x .

Table 3. Sediment wave size classification scheme used in this study. Source: Van Landeghem, et al., [56] and Evans, et al., [79], originally adapted from Ashley [46] and Berne, et al., [80].

Sediment Wave Classification	Height (m)	Wavelength (m)
Small	0.04–0.25	0.6–5
Medium	0.25–0.44	5–10
Large	0.44–2.8	10–100
Very large	>2.8	>100

3.2.2. Sand Wave Migration Direction and Rates

Previous studies calculated migration rate over two-dimensional (2-D) cross-sectional profiles perpendicular to the crest [4,30]. These provide a good estimate of migration rate and direction in localised areas, but fail to represent changes in rate and direction along the crest and in the wider assemblage and give a more regional view of the sediment transport system and hydrodynamic drivers. This study calculates migration direction and rates through an iterative process using a combined method in GRASS GIS v.7.6.1, QGIS v.3.8.1 and ArcGIS v.10.8.

The methodology of Di Stefano and Mayer [81] for extracting sediment wave crests by geomorphon analysis [73] was adapted by this study. Georeferenced polyline shapefiles of delineated sediment wave crests in plan-view were produced from each individual bathymetric raster dataset (Table 2). These datasets were quality controlled (QC) in ArcGIS v.10.8 using the slope and Terrain Ruggedness (VRM) tool [72]. Taking two time-lapse shapefiles at a time and starting with the earlier time-step, several steps were taken to calculate the direction and magnitude of sediment wave crest displacement over time (Figure 3) in ArcGIS v.10.8 and QGIS v.3.8.0. A step-by-step guide can be found in the

supplementary material to this article. Annual migration rates along the crest of each sediment wave were subsequently calculated based on the dates of each survey.

Crest perpendicular cross-sections were extracted from time-lapse bathymetric datasets for further morphological and geomorphological analysis. This study uses a combination of the two-part geomorphological classification scheme developed by Dove, et al., [82] and the classification scheme adopted by Van Landeghem, et al., [56]. Digital Elevation Models (DEM) of difference (DOD) were calculated to quantify the volumetric change between successive bathymetric surveys, highlight geomorphic changes in a three-dimensional (3-D) surface, and QC sediment wave migration directions. This aided the quantification of change in a one-dimensional (1-D), 2-D, and 3-D manner, allowing for a better understanding of bedform development across a sediment wave assemblage. This allows the interpretation of trends in the wider hydrodynamic-morphodynamic system.

3.3. Sediment Samples

Surficial sediment samples were collected using either the Day Grab sampler or the Shipek sampler during the three MOVE survey campaigns (Figure 2). All sediment samples were processed by sieving or laser granulometry. Furthermore, sediment samples containing raw granulometric data was compiled from Geological Survey of Ireland (GSI). The MOVE and GSI datasets were combined, and statistical analysis was carried out using the R package ‘geotech’ [83]. The resulting median grain size, D_{50} , values were interpolated into a raster dataset in ArcGIS v10.8. This raster dataset is used for two levels of analysis:

(a) At an individual site level: The resulting point file produced from the Wang, et al., [78] method (Section 3.2.1), that delineates the crest of sediment waves in each of the 17 sites (Figure 2), is used to extract D_{50} values from the interpolated raster. These extracted values are used in the investigation of statistical relationships between individual sediment wave dimensions and environmental parameters/processes such as median grain size, D_{50} , and Rouse number, P (which indicates the mode of sediment transport).

(b) At a coarse level to elucidate the dynamics of the wider sediment transport system. The raster dataset was interpolated onto a 500 m resolution point grid, covering the entire south-western Irish Sea region. This dataset was used to calculate P , entrainment function, F_s , and shear Reynold’s number, Re_* . Formulae used are presented in Section 3.5.

3.4. Hydrodynamic Modelling

A validated, two-dimensional, hydrodynamic model covering the entire Irish Sea, developed using the Danish Hydraulics Institute’s MIKE 21 suite of tools [84,85], was used to simulate bed shear stress and tidal current u and v magnitude components for a one-month period. Model set-up and validation is published in Coughlan, et al., [64].

The hydrodynamic model [85] determines bottom shear stress, τ_b , by quadratic friction law:

$$\tau_b = C_d \rho \bar{U}^2 \quad (3)$$

where C_d is a drag coefficient, ρ is the density of the fluid medium in seawater, and \bar{U} is the depth averaged velocity. The drag coefficient is determined as;

$$C_d = \frac{g}{(Mh^{1/6})^2} \quad (4)$$

where h is the total water depth, g is the acceleration due to gravity, and M is the Manning number. A constant Manning number of $32 \text{ m}^{(1/3)}\text{s}^{-1}$ was applied in this case. Model outputs were interpolated on to a 1 km^2 grid where the residual bed shear stress and residual tidal currents were calculated. These datasets were used by Creane, et al., [5] and used again in this study.

Raster datasets of mean and maximum current velocities, produced by Coughlan, et al., [64] were also used in this study.

All four datasets were interpolated onto the same two shapefiles as grain size data in Section 3.3, i.e.:

- (a) the 500 m resolution matrix, for coarse level theoretical parameter calculations, and
- (b) the resulting point shapefile produced from the Wang, et al., [78] method in Section 3.2.1., for investigation into the relationship between environmental parameters and individual sand wave dimensions.

3.5. Theoretical Parameters

The Rouse number, P , which indicates the mode of sediment transport is calculated similar to that of Borsje, et al., [60],

$$P = \frac{w_s}{1 \times 0.40 \times u_*} \quad (5)$$

where w_s is the particle settling velocity according to Allen's Law,

$$w_s = \frac{0.153 \times [(\rho_s - \rho) \times g]^{0.714} \times D_{50}^{1.143}}{\mu^{0.430} \times \rho^{0.286}} \quad (6)$$

where ρ_s is the density of particle, ρ is the density of a fluid, g is the acceleration due to gravity, μ is the dynamic viscosity of a liquid, D_{50} is the median grain size, and u_* is the shear velocity according to

$$u_* = \sqrt{\frac{\tau_b}{\rho}} \quad (7)$$

where τ_b is the bottom shear stress as given in Section 3.4 under tidal current only. In this case, C_d is calculated as below

$$C_d = \left[\frac{k}{\ln\left(\frac{h}{z_0}\right) - 1} \right]^2 \quad (8)$$

where h is water depth, k is the von Karman constant, and z_0 is the hydraulic roughness given from the following equation

$$z_0 = \frac{2.5 \times D_{50}}{30} \quad (9)$$

Bedload transport is dominant when $P > 2.5$, whereas suspended load transport is the dominant mode when $0.8 < P < 1.2$.

Shields [86] found that a plot of the entrainment function, F_s , against the shear Reynolds number, Re_* , produced a useful chart for predicting the threshold of motion and bedform type when threshold conditions are exceeded. The entrainment function is the ratio of the lift force on a sediment particle to its submerged weight, given by

$$F_s = \frac{\tau_b}{\left(\frac{\rho_s}{\rho} - 1\right) \rho g D_{50}} = \frac{u_*^2}{\left(\frac{\rho_s}{\rho} - 1\right) g D_{50}} \quad (10)$$

The shear Reynolds number is proportional to the ratio of the sediment particle diameter to the thickness of the viscous sub-layer

$$Re_* = \frac{u_* D_{50}}{\nu} \quad (11)$$

Where critical shear stress is exceeded by bottom shear stress, sediment is mobilised. The Mobilisation Frequency Index (MFI), developed by Coughlan, et al., [64], showing the yearly exceedance of critical shear stress (τ_{cr}) under current-induced (τ_c) and combined current- and wave-induced bed shear stress (τ_{cw}), is used in this study.

4. Results

4.1. Sand Wave Characteristics

4.1.1. Sediment Wave Shape

Figure 4 exhibits the variation of sediment wave shape across the south-western Irish Sea. The morphological definition is two-fold, with waves occurring as either asymmetric (i.e., progressive) or symmetric (i.e., trochoidal), and with crests that are either round, sharp and/or bifurcating. Sediment waves can be compound (superimposed by smaller sediment waves) or simple, and occur in two- or three-dimensional form.

These morphological characteristics often occur within the same sediment wave field and/or environment, and frequently change over time between time-lapse survey intervals, for example, the same sediment wave may transition from round- to sharp-crested or from simple to compound or vice versa. An example of each of these types is represented in Figure 5.

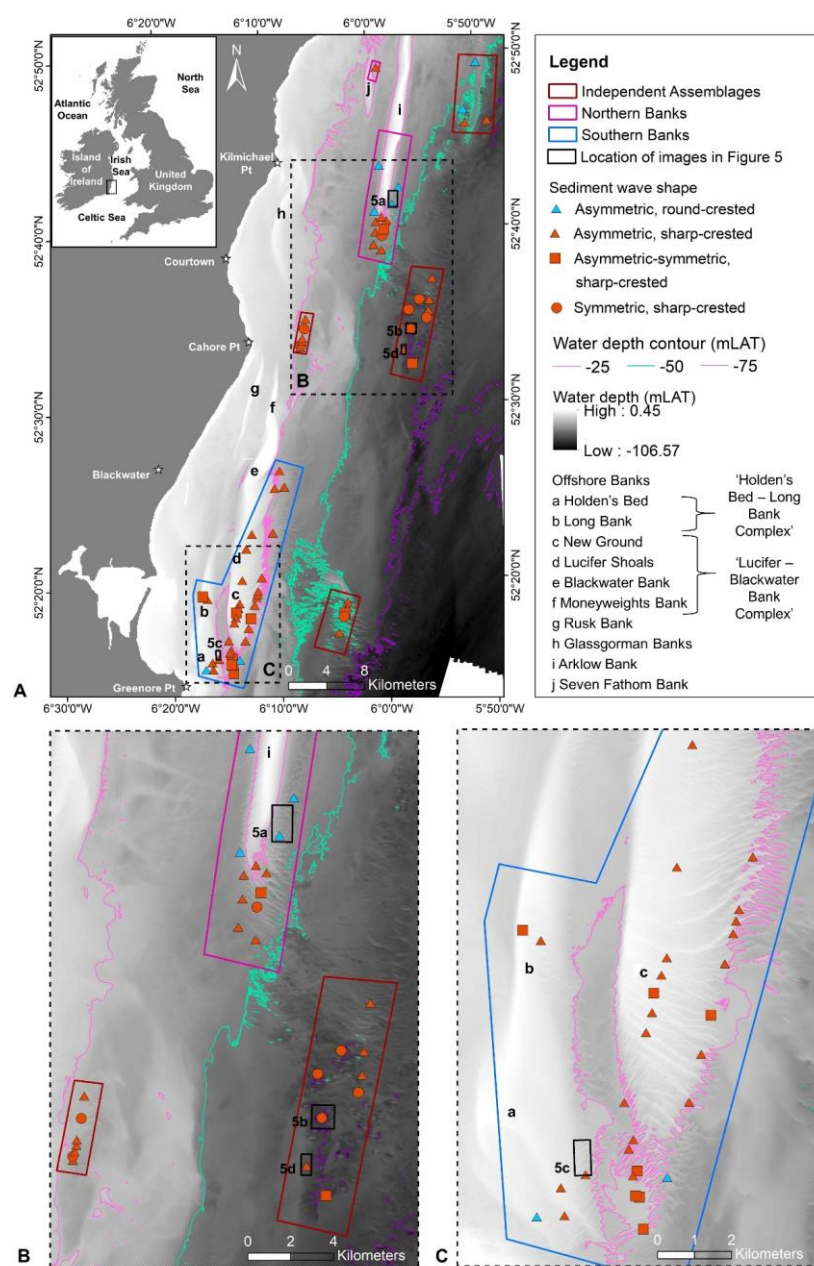


Figure 4. Interpreted average sediment wave shape across the south-western Irish Sea. The location of (B) and (C) are provided in (A). Black boxes and labels indicate the location of figures in Figure

5. Bathymetry source: composite map produced from INFOMAR datasets (<https://www.infomar.ie/data> [Accessed: 10 June 2021]) (see Section 3.1).

Independent sediment wave assemblages display predominately round- to sharp-crested, asymmetric sediment waves, interspersed with very large sharp-crested trochoidal sediment waves. Sediment waves associated with sand banks display a much greater variance in sediment wave type over a relatively small spatial extent in comparison to these independent wave fields (Figure 4).

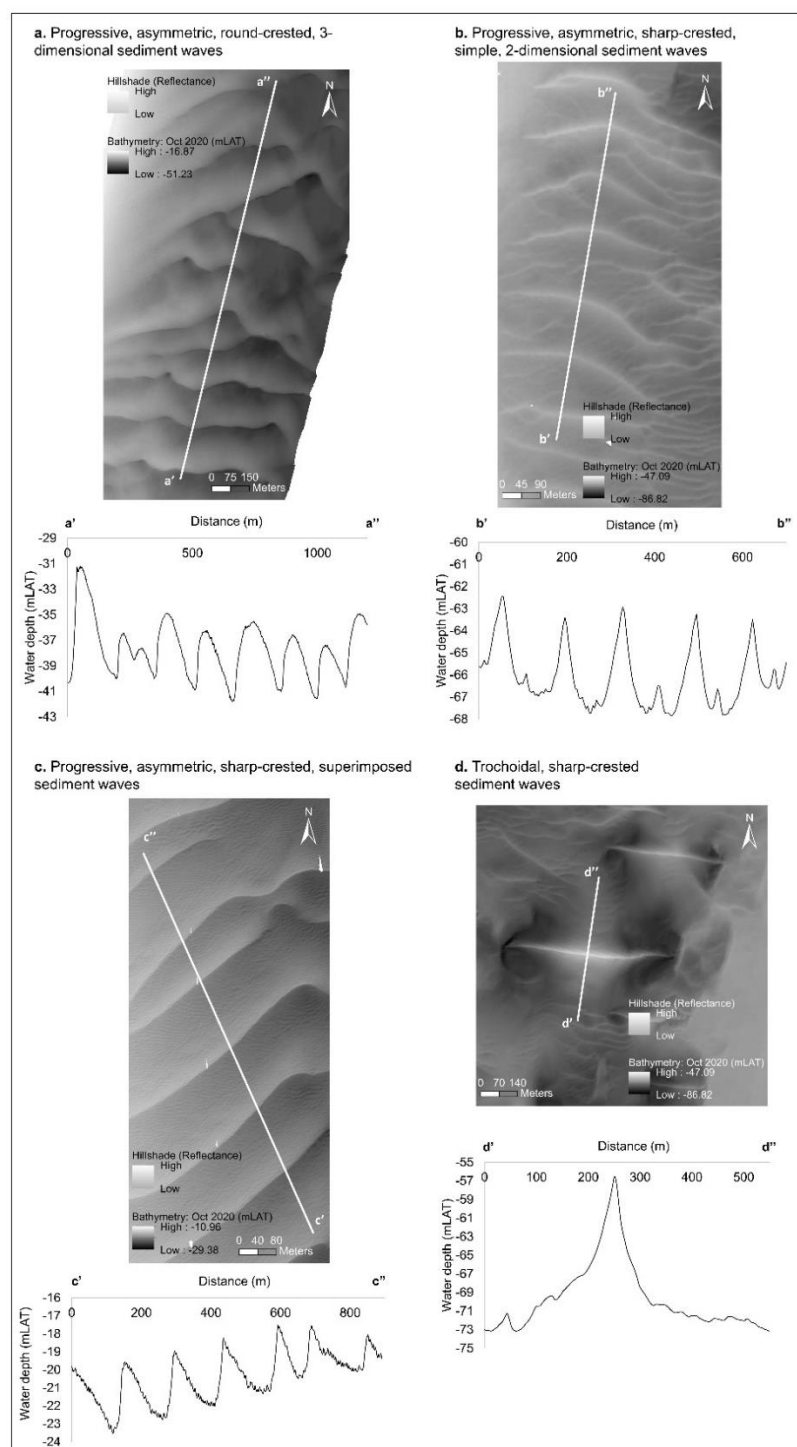


Figure 5. Selection of sediment wave types observed in the south-western Irish Sea; a. progressive, asymmetric, round-crested, 3-dimensional sediment waves, b. progressive, asymmetric, sharp-

crested, simple, 2-dimensional sediment waves, c. progressive, asymmetric, sharp-crested, superimposed sediment waves, and d. trochoidal, sharp-crested sediment waves. A representative cross-section is given for each type. Locations are given in Figure 4. Bathymetry source: MOVE 2020 survey (see site 1A, 6, and 3A in Table 2).

4.1.2. Sediment Wave Dimensions

Analysed sediment waves occur in a range of water depths from 8.2 to 83 mLAT, exhibiting wave heights and wavelengths ranging from 0.1 to 25.7 m and 17 to 983 m respectively. A summary of sediment wave dimensions for each individual site is given in Table 4. Markedly, the highest maximum sediment wave heights occur in independent sediment wave assemblages at sites 5 and 6 (Figure 2). These large dimensions correspond to very large, isolated trochoidal sediment waves. Contrastingly, the largest maximum wavelength values are evident along the eastern slope of Lucifer Bank at sites 2D and 2E. These large wavelengths are connected to a sequence of relatively large sediment waves, or transverse sediment ridges, extending in a curvilinear form from the sand bank crest to bank base. However, as shown in Table 4, these very large sediment waves do not represent the entirety of the sites and are instead encompassed by relatively smaller large- to very-large sediment waves with a mean wave height of 2.9 to 4.7 m (at sites 2D and 2E) and mean wavelength of 157.4 to 215.1 m (at sites 5 and 6). These morphological variations will be discussed further in Sections 4.2.2.1. and 5.1.2.

Table 4. Sediment wave characteristics for each individual study site based on first time-lapse bathymetric dataset.

Site		Wave Height (m)	Wave Length (WL) (m)	Left WL (m)	Right WL (m)	Asymmetry	Steepness	Average Lee Slope Angle (°)	Water Depth (mLAT)	D50 (mm)
7	mean	2.1	114.5	65.1	49.4	0.12	0.019	3.0	30.2	0.3
	max	5.2	355.0	213.0	241.0	0.72	0.053	9.3	32.5	0.5
	min	0.3	43.0	10.0	14.0	−0.82	0.002	0.3	27.5	0.2
2A	mean	2.4	142.2	60.8	81.4	−0.14	0.018	2.9	30.2	0.4
	max	7.5	474.0	343.0	337.0	0.82	0.060	16.1	38.8	0.8
	min	0.2	22.0	4.0	7.0	−0.92	0.001	0.0	18.8	0.2
2B and 2C	mean	4.0	150.2	90.3	59.9	0.18	0.027	4.6	26.3	0.6
	max	11.7	494.0	446.0	280.0	0.82	0.069	14.2	38.1	2.2
	min	0.6	30.0	5.9	12.0	−0.87	0.002	0.5	13.1	0.3
2D	mean	4.7	215.1	114.4	100.6	0.06	0.023	3.8	25.3	1.2
	max	11.7	813.0	620.0	617.1	0.84	0.085	11.6	44.9	1.9
	min	0.7	59.0	9.0	11.9	−0.89	0.002	0.4	11.6	0.4
2E	mean	2.9	157.4	76.4	81.1	−0.04	0.021	3.3	25.4	1.1
	max	12.3	983.0	842.0	883.0	0.91	0.071	16.0	38.5	2.6
	min	0.4	28.3	5.0	4.0	−0.90	0.001	0.3	8.2	0.3
3A and 3B	mean	1.5	126.1	67.6	58.5	0.04	0.013	2.1	20.2	0.8
	max	6.3	281.0	239.0	224.1	0.83	0.063	11.9	29.2	1.5
	min	0.2	30.0	4.0	7.0	−0.91	0.001	0.2	9.3	0.3
1A	mean	3.0	140.2	56.3	83.9	−0.19	0.022	4.1	34.7	0.8
	max	15.2	421.0	310.0	335.0	0.88	0.083	27.3	52.2	5.0
	min	0.2	28.0	5.0	4.0	−0.92	0.001	0.1	15.8	0.3
1B	mean	4.7	165.4	80.5	84.9	−0.02	0.029	4.7	38.0	0.3
	max	18.1	581.0	442.0	481.0	0.84	0.092	18.0	51.1	0.9
	min	0.6	33.0	9.9	10.9	−0.89	0.003	0.2	19.1	0.1
1C	mean	2.3	123.5	56.6	66.9	−0.06	0.020	3.2	26.1	0.3
	max	7.5	422.1	242.1	338.0	0.91	0.082	15.6	39.7	0.8

	min	0.2	26.0	6.0	4.0	-0.87	0.001	0.0	8.5	0.1
4	mean	0.6	124.8	63.9	60.9	0.02	0.005	0.9	28.7	0.4
	max	1.2	291.0	240.0	229.0	0.70	0.016	3.2	29.7	0.7
	min	0.1	50.0	13.0	12.0	-0.65	0.001	0.1	27.1	0.3
5	mean	6.1	216.7	106.5	110.2	-0.02	0.029	4.8	57.9	0.6
	max	23.5	681.0	505.0	576.1	0.86	0.088	17.4	72.9	2.3
	min	0.9	52.0	4.9	13.0	-0.91	0.002	0.5	36.6	0.2
6	mean	4.7	163.7	77.2	86.5	-0.05	0.030	4.8	65.9	1.3
	max	25.7	614.0	428.1	460.1	0.80	0.120	23.0	83.0	5.0
	min	0.4	34.0	5.9	9.9	-0.90	0.002	0.5	52.8	0.3
3C	mean	1.4	101.8	51.5	50.3	0.00	0.015	2.5	18.7	1.0
	max	3.7	313.0	196.0	213.0	0.77	0.044	8.5	26.8	2.8
	min	0.2	29.0	3.0	9.0	-0.87	0.001	0.0	10.4	0.8
2F	mean	1.5	174.9	62.9	112.0	-0.27	0.009	1.8	11.2	0.8
	max	4.4	599.0	336.0	391.0	0.73	0.043	8.0	14.2	1.1
	min	0.2	45.0	9.0	22.0	-0.92	0.001	0.1	7.8	0.3
8	mean	3.4	159.8	93.6	66.3	0.11	0.022	3.7	53.5	0.5
	max	10.2	478.0	365.1	303.0	0.83	0.068	15.4	72.0	1.0
	min	0.1	17.0	3.0	5.0	-0.87	0.001	0.3	40.0	0.3

Table 5 and Figure 6 display the power regression relationship between sediment wave height and wavelength for (i) the full dataset, (ii) three separate environments, and (iii) each individual study site (Figure 2; Figure 3). The full dataset and each environment show moderate to strong positive relationships ($r = 0.52$ to 0.71) between these two parameters, indicating a relatively large scatter of data points. The relationship derived from the full dataset ($H_{mean} = 0.03L^{0.90}$) is relatively lower than the power relation described from the global dataset ($H_{mean} = 0.0677L^{0.8089}$), yet almost identical to that found by Francken, et al., [62] (Table 1). Sediment waves at both the northern banks and independent assemblages display similar relationships to the full dataset yet the southern banks display a relatively higher relationship of $H_{mean} = 0.05L^{0.77}$, correlating well with the relationship derived from giant sand waves on the Taiwan Banks, in the Taiwan Strait [4] (Table 1).

On an individual site level, sediment wave assemblages associated with sediment banks display relatively higher power relationships in comparison to those independent from larger bedforms, i.e., sites 5, 6, and 8. These higher relationships grow closer to the upper limit of sand wave growth ($H_{max} = 0.16L^{0.84}$) defined by Flemming [48]. Additionally, these higher relationships correlate better with the height-spacing power-law relationships derived by Van Landeghem, et al., [56] in the Irish Sea under different depth intervals: (a) 20–30 m ($H = 0.1082L^{0.6174}$, $r = 0.870$), (b) 20–40 m ($H = 0.0921L^{0.6651}$, $r = 0.856$), and (c) 20–60 m ($H = 0.0921L^{0.6651}$, $r = 0.869$). Site 2D exceeds this upper limit with a moderate positive correlation ($r = 0.43$).

Table 5. Relationship between bedform heights and wavelengths in the south-western Irish Sea. The Full dataset has been broken into three environments i.e., Southern Banks, Northern Banks and Independent Assemblages, and each individual study site.

Dataset	Power Regression Equation	r^2	Correlation Coefficient (r)	Correlation Description
Full dataset	$H_{mean} = 0.03L^{0.90}$	0.33	0.58	Moderate positive
Southern Banks	$H_{mean} = 0.05L^{0.77}$	0.27	0.52	Moderate positive
Northern Banks	$H_{mean} = 0.02L^{0.95}$	0.28	0.52	Moderate positive
Independent Assemblages	$H_{mean} = 0.03L^{0.96}$	0.50	0.71	Strong positive
8	$H_{mean} = 0.03L^{0.91}$	0.53	0.73	Strong positive

2F	$H_{mean} = 0.08L^{0.56}$	0.15	0.39	Weak positive
3C	$H_{mean} = 0.12L^{0.52}$	0.12	0.34	Weak positive
6	$H_{mean} = 0.04L^{0.92}$	0.48	0.69	Strong positive
5	$H_{mean} = 0.06L^{0.83}$	0.38	0.62	Strong positive
4	$H_{mean} = 0.29L^{0.13}$	0	0.07	Very weak positive or no association
1C	$H_{mean} = 0.08L^{0.78}$	0.30	0.55	Moderate positive
1B	$H_{mean} = 0.10L^{0.63}$	0.14	0.38	Weak positive
1A	$H_{mean} = 0.01L^{1.04}$	0.30	0.55	Moderate positive
3A and 3B	$H_{mean} = 0.06L^{0.64}$	0.13	0.36	Weak positive
2E	$H_{mean} = 0.11L^{0.63}$	0.31	0.56	Moderate positive
2D	$H_{mean} = 0.22L^{0.55}$	0.19	0.43	Moderate positive
2B and 2C	$H_{mean} = 0.11L^{0.71}$	0.31	0.56	Moderate positive
2A	$H_{mean} = 0.07L^{0.69}$	0.26	0.51	Moderate positive
7	$H_{mean} = 0.08L^{0.67}$	0.19	0.43	Moderate positive

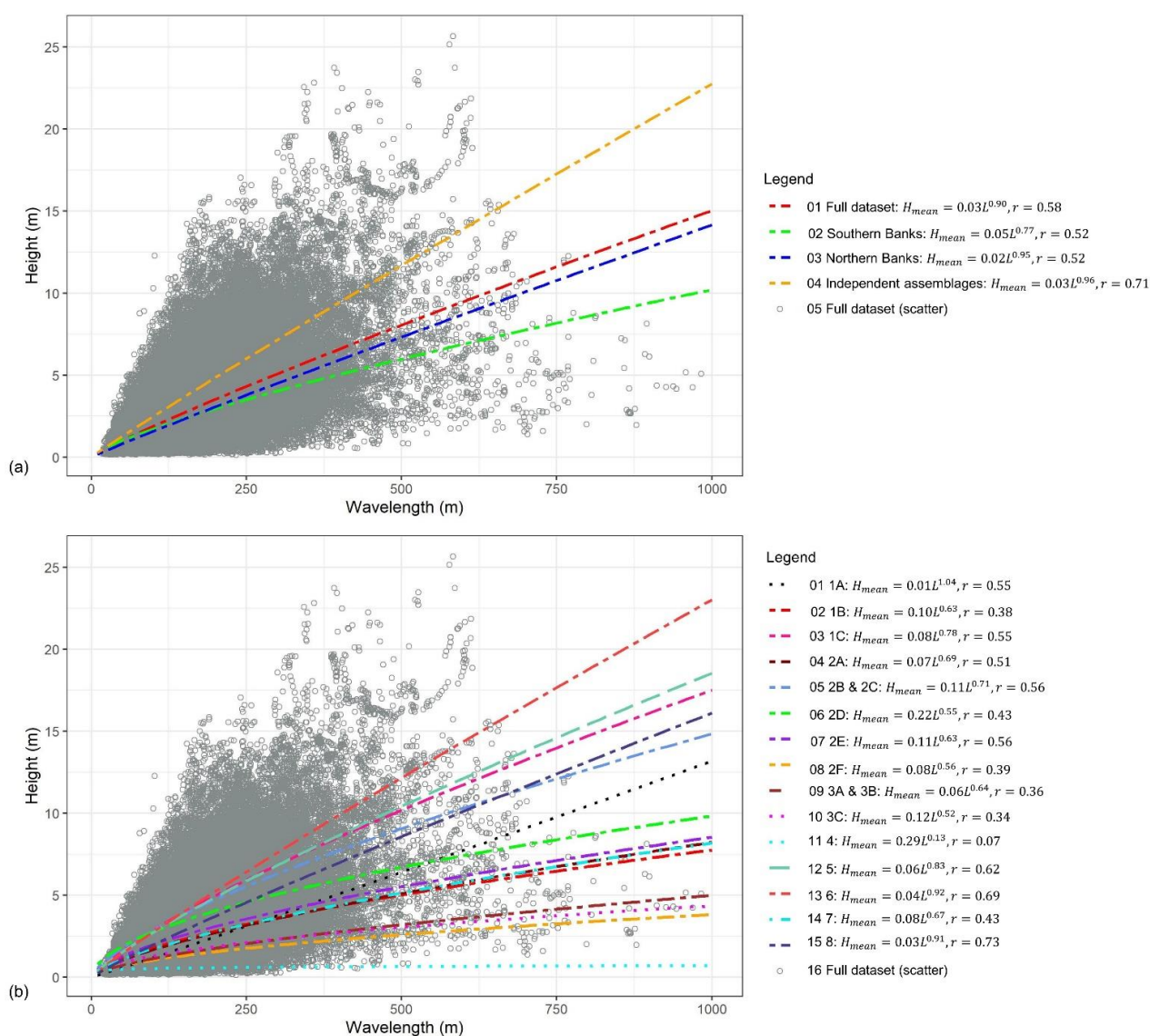


Figure 6. Relationship between sediment wave heights and wavelengths in the south-western Irish Sea: (a) displays the results for the full dataset and for three compiled environments i.e., Southern Banks, Northern Banks and Independent Assemblages, and (b) displays the results for each individual study site.

4.2. Spatial and Temporal Evolution of Sediment Waves

Figure 7 presents the average annual sediment wave migration directions and rates, derived from plan-view crest displacement over time. Each arrow in Figure 7 accurately represents the average migration parameter of a set of consecutive sediment waves (Figure 3) travelling in the same direction and approximately at a similar rate.

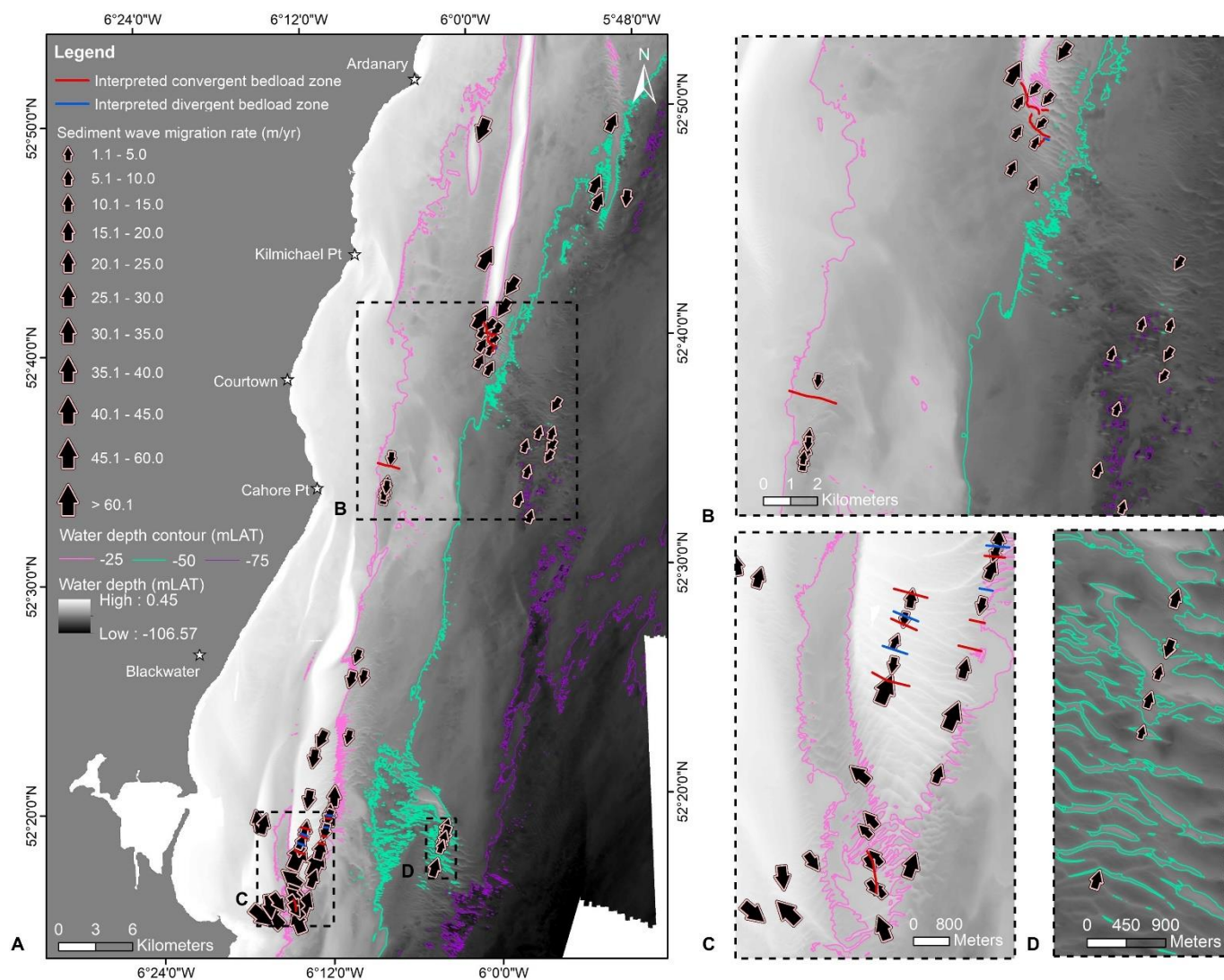


Figure 7. Average annual sediment wave migration rates updated with new time-lapse multi-beam echo sounder bathymetry datasets: (A) an overview of south-western Irish Sea, whereby the locations of (B) to (D) are indicated; (B) inset of study sites 1, 6 and 7; (C) inset of study sites 2 and 3; (D) inset of study site 5. See Figure 2 for study site boundaries. Figure bathymetry data source: composite map produced from INFOMAR datasets (referenced to Lowest Astronomical Tide (LAT)) (<https://www.infomar.ie/data> [Accessed: 10 June 2021]) (see Section 3.1).

At many study sites, time intervals between various time-lapse bathymetry datasets were too long to accurately derive migration parameters. This was predominately due to: (a) sediment waves had migrated more than one wavelength and so could not be accurately identified as the same wave in two consecutive datasets, or (b) the sediment wave had undertaken a significant amount of morphological change (e.g., crest deterioration, amalgamation of two sediment waves), and so the same wave could not be identified in consecutive datasets. Nevertheless, at each location at least two bathymetric datasets could be used to accurately measure migration parameters. Newly identified local con-

vergence and divergence zones are also delineated. Distinct spatial and temporal variability and morphological evolution observed at each site will be described in more detail in the following sections.

4.2.1. Sediment Waves Associated with Arklow Bank

On the south-east side of Arklow Bank, a progressive, asymmetric, round-crested, irregular sediment wave assemblage migrates in a south-westerly direction at a rate of 23 m/yr (Figure 8). These very large sediment waves transition abruptly from an irregular assemblage that is limited to the lower slope and base of the bank, to a regular assemblage that covers a larger spatial area, extending eastward from the bank crest to bank base.

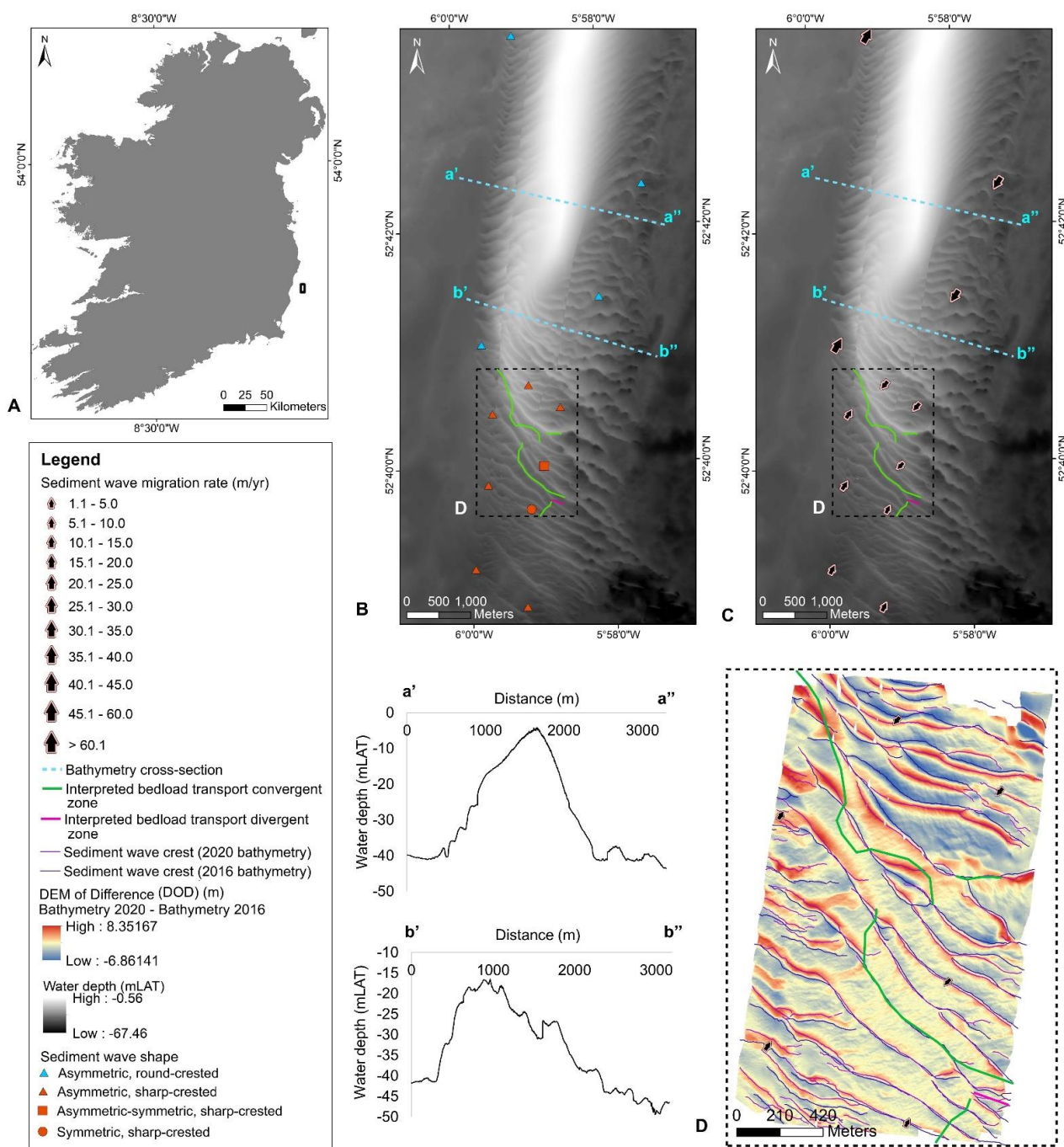


Figure 8. Sediment wave translation rates and shapes at the southern extent of Arklow Bank in the Irish Sea: (A) location of Arklow Bank; (B) sediment wave shape with locations of cross-sections a

and b; (C) and (D) sediment wave translation rates. (B) and (C) bathymetry source: composite map produced from INFOMAR datasets (<https://www.infomar.ie/data> [Accessed: 10 June 2021]) (see Section 3.1). (D) bathymetry source: 2016: INFOMAR survey; 2020: MOVE survey (see site 1B in Table 2).

This abrupt transition correlates with a sudden change in sand bank morphology at its southern end. Sand bank height is markedly reduced whilst wavelength is increased, revealing a more elongated, subdued asymmetric shape (Figure 8). This is associated with increased water depth at the bank crest and a distinct westward facing lee slope indicating a potential westward migration at this section. Sediment wave crests extend along the entire length of the bank's stoss slope, changing progressively from a perpendicular to curvilinear alignment to the bank crest. Specifically, sediment waves display a distinct reduction in migration rate from 23 m/yr to 8.5 m/yr where the crest alignment transitions from E–W to SSE–NNW. Additionally, this combined migration rate reduction and crest orientation change marks a distinct morphological change in the sediment wave assemblage from round- to sharp-crested. Migration rate continues to reduce from 2.8 m/yr to almost zero mobility at a curvilinear convergence zone (Figure 8), whereby these southward migrating bedforms are met with a northward flowing assemblage. This convergence zone is marked by a relatively larger, sharp-crested, symmetrical, curvilinear sediment ridge, marking a build-up of sediment (accretion) in this zone. This ridge is bound on either side by asymmetrical waves moving in the opposite directions, which grow progressively more asymmetric with increasing distance from the convergence zone.

South of this convergent zone on the eastern side of the bank, a progressive, sharp-crested, symmetric to slightly asymmetric sediment wave assemblage, migrates northwards towards the convergent zone at an average rate of 2.5 m/yr. Moving westwards and north-westwards along the convergent line, on the outer edge of the sediment wave assemblage, asymmetric sediment waves move northwards at a higher rate of 9.8 m/yr. South of this region, the sand bank flattens more rapidly, water depth increases progressively, and northward migrating sediment waves (at 8.1 m/yr) are asymmetric, progressive, and sharp-crested. Furthermore, at the foot of the lee slope of the bank, where there is an increase in sediment wave northward migration rate (9.8 m/yr to 32.7 m/yr), a distinct morphological change from sharp-crested sediment waves to round-crested sediment waves is observed. This is consistent with the sudden morphological changes on the stoss slope. These lee-slope northward migrating waves migrate faster (32.7 m/yr) than southward moving waves on the stoss slope (23 m/yr). They continue migrating northwards at an average rate of 32.7 m/yr on the lee slope.

On both sides of the bank, in plan-view, sediment wave crests markedly alter their orientation from approximately E–W to SW–NE when transitioning from base to slope. Ultimately, the sediment wave crest orientation adjusts to a curvilinear configuration to adjust progressively towards parallel alignment with the bank crest. However, except for the southern extent of the bank where its morphology becomes more subdued, no sediment waves have been observed reaching the crest of the bank. This may be due to limited water depth and complex hydrodynamic and wave climate conditions.

4.2.2. Sediment Waves Associated with Lucifer–Blackwater Bank and Holden's Bed–Long Bank Complexes

Southern Extent of Lucifer–Blackwater Bank Complex

Sediment waves in the southern section of Lucifer–Blackwater Bank complex (sites 2D, 2E, and 2F) (Figure 2) are highly mobile and highly morpho-dynamic whereby their shape, migration direction and migration rate progressively change throughout the study area (Figure 9). In contrast to Arklow Bank, the southern section of the Lucifer–Blackwater Bank complex does not display an anticlockwise circulatory bedform migration pattern around the bank itself. Instead, sediment waves migrate approximately north-westwards and north-eastwards on the western and eastern sides of the bank respectively (Figure

9B). This general northward migratory trend becomes increasingly intricate with addition of the following observations:

(a) the presence of a clear reversal in sediment wave migration direction or ‘pivoting’ phenomenon over an approximate 1000 m transect on the lower slope of the south-western side of the bank (Figure 9D),

(b) the presence of multiple reversals in migration direction that ultimately generate a localised, complex sediment transport convergence and divergence pattern within a restricted area (over approximately 2400 m) on the south-eastern side of the bank (Figures 9B and 8C), and

(c) the dominant north-eastward moving bedforms are met with a dominant southward sediment transport pathway originating along the Blackwater Bank (‘F’ in Figure 9B).

These three observations will be discussed in detail.

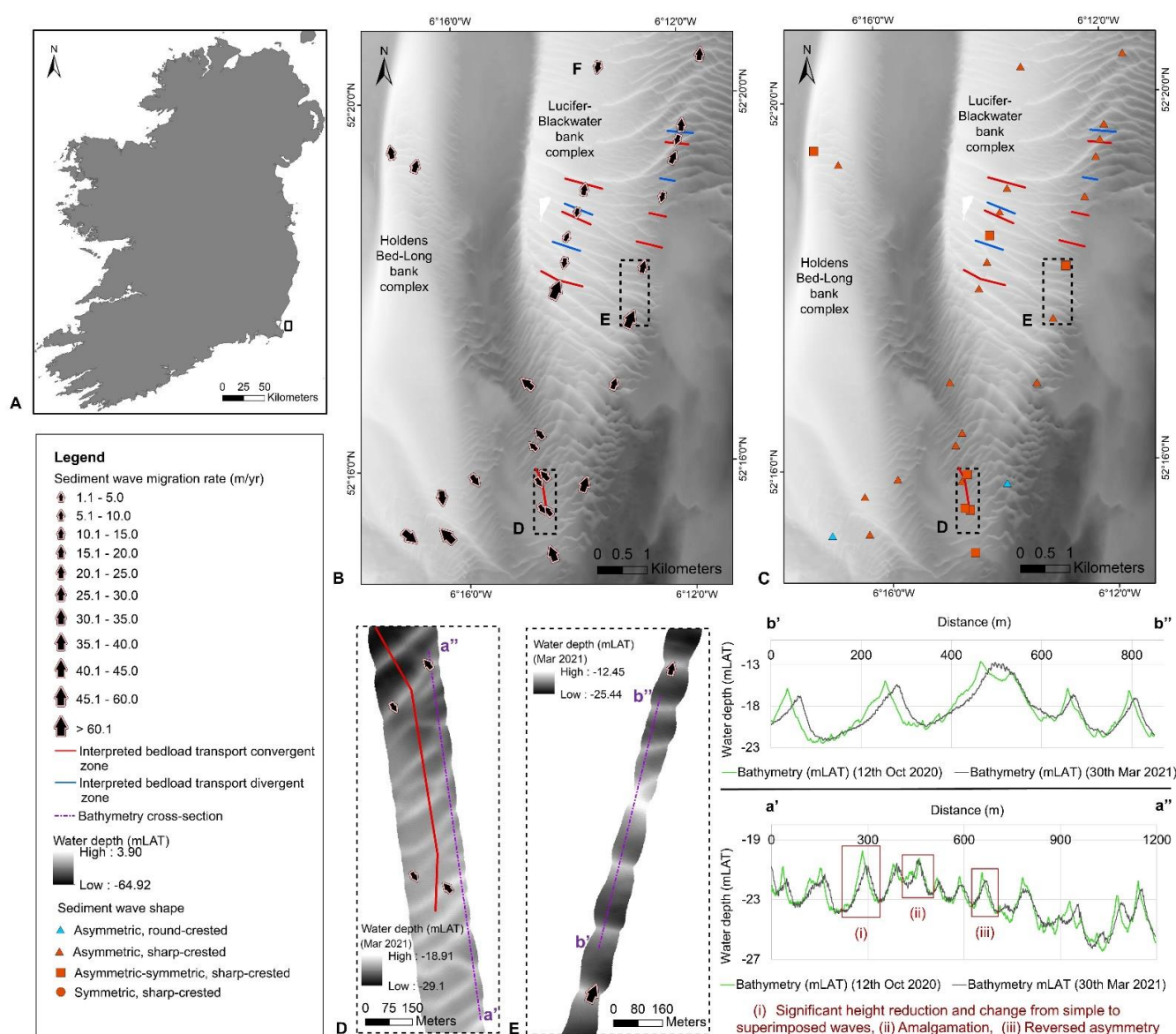


Figure 9. Sediment wave dynamics at the southern extent of Lucifer–Blackwater Bank and Holden’s Bed–Long Bank complexes. (A) Location of analysed site. (B) Distribution of sediment wave migration direction and rates. (C) Distribution of sediment wave shape. B and C bathymetry source: composite map produced from INFOMAR datasets (<https://www.infomar.ie/data> [Accessed: 10 June 2021]) (see Section 3.1). (D) Cross-section ‘a’ location. (E) Cross-section ‘b’ location. D and E bathymetry source: site 2E in Table 2.

Lucifer Bank is asymmetric, with its lee and stoss slope facing westward and eastward (offshore) respectively. In plan-view, sediment wave crests at the southern extent of the bank are orientated at an inclined angle (NW–SE and NE–SW on the stoss and lee slopes respectively) so that they join at an acute angle at the bank crest. This connection point suggests a potential convergence zone. Nevertheless, this pattern is not continued throughout the central and northern extent of the Lucifer–Blackwater Bank complex, instead the sediment waves diminish towards the bank crest and are relatively absent on the lee slope.

These sediment waves on the southern extent of the bank have migrated more than one wavelength between the 2009 and 2020 bathymetric surveys therefore migratory patterns and morphological changes could not be resolved over this time frame. Consequently, the observations presented here are from the analysis of a long stretch of repeat time-lapse swath bathymetry data (October 2020 and March 2021) that is approximately 200–400 m wide.

The most southwestern section of the site reveals slightly asymmetric to symmetric sediment waves moving north-westward at approximately 37.7 m/yr (sand wave migration vector directly south of inset 'D' in Figure 9B). Approximately 800 m north westwards of this, sediment waves transition into more symmetrical shape and exhibit a bi-directional migration pattern (Figure 9D). The section of the sediment wave crests closest to the bank crest continues to move northwards at an average rate of 19.8 m/yr, yet the section of the same sediment wave crests closer to the bank base migrates southwards at an average rate of 13.9 m/yr. This generates a pivoting motion along each sediment wave crest over an approximate 1000 m transect. At the meeting point of these pivoting crests there is a very slow to no migration zone. Sediment waves tend to be symmetrical and may indicate a convergence or a coincidence of opposite moving sediment transport pathways (Figure 9D). This pivoting phenomenon of the sediment wave crests is like that revealed at the southern end of Arklow Bank. This trend extends approximately 1000 m until the bedforms reverse back to a north-westward migratory direction.

At this transition point, the sediment wave assemblage continues to move at a differential migration rate, with slower rates (14 m/yr) exhibited towards the bank base and faster rates (19.8 m/yr) towards the bank crest. Sediment waves progressively return to a relatively constant rate of 34.2 m/yr, continuing in this north-westward direction.

Significant sediment wave morphological changes over time are observed in this area, which help to provide insight into the sediment wave growth and development processes in a complex tidal current regime. Between the 2009 and 2020 datasets, bedforms could not be compared like for like as migration has been greater than one wavelength. However, over this time interval, the general symmetrical to slightly asymmetrical shape of sediment waves are maintained, and bedforms remain simple (not superimposed) and sharp-crested. Contrastingly, from 2020 to 2021, morphological changes are evident. Over this time period, sediment waves show similar symmetric to slightly asymmetric shape/bedform profile; however a slight increase in their asymmetry into the direction of migration is evident. Some sediment waves notably migrate in the opposite direction to asymmetry. In this case, their asymmetry in the first time-step is in the opposite direction to their migratory direction, however in the second time-step, their asymmetry changes to slightly asymmetric in the direction of migration (cross-section a in Figure 9D). In 2020, bedforms are simple and sharp-crested, yet in 2021 they become compound waves (superimposed by smaller sediment waves) with bifurcating crests. Additionally, there is a notable sediment wave height decrease over the 169-day period. Amalgamation of smaller waves into larger waves is common, potentially indicating a growth mechanism (cross-section a in Figure 9D).

At the south-eastern section of the Lucifer–Blackwater Bank complex (site 2E (Figure 2)), round-crested, symmetric to slightly asymmetric, widely spaced (~200 m) sediment waves migrate north-eastward at an average rate 36 m/yr (Figure 9B and C). Approxi-

mately 2000 m north-east from the southern tip of the assemblage, these bedforms abruptly decrease to an average migration rate of 16 m/yr. This decrease is directly correlating with three morphological changes: (i) an increase asymmetry (in the direction of migration), (ii) a change from round- to sharp-crests, and (iii) a transition from wide to tightly spaced rhythmic bedforms. These dramatic morphological changes are consistent in all three time-lapse geophysical surveys.

A significant increase in migration rate from 16 m/yr to 59.1 m/yr (in 18 mLAT water depth) is observed north of this section (site 2D (Figure 2)), moving in a similar north-eastward direction (Figure 9B,C). These lower slope observations coincide with high average migration rates of 71.6 m/yr observed along the same sediment wave crest on the upper slopes of the bank (site 2F (Figure 2)), in approximately 11 mLAT water depth. Similar morphological changes are resolved compared to previous sections. Bedform asymmetry remains in the direction of migration. Sediment waves in 2009 and 2020 tend to be compound and sharp-crested. However, from 2020 to 2021, there is notable slight rounding of the crests, an amalgamation of sediment waves, and averaged bedform heights are reduced.

A decrease in north-eastward sediment wave migration rate along this pathway from 59 m/yr to an average of 21 m/yr is observed. This reduction is marked by a relatively larger sediment wave/transverse ridge and a notable increase in bed level indicating sediment accretion (cross-section b in Figure 9E). Sediment waves remain asymmetric in direction of asymmetry.

From this point, a sediment transport convergence and divergence pattern are observed along a 500–900 m SSW–NNE trending transect (Figure 9B,C). North-westward migrating sediment waves notably transition gradually from asymmetric to symmetric and back to asymmetric in the opposite direction. A distinct migration directional change is associated with these morphological observations whereby bedforms migrate south-westwards at an average rate of 11 m/yr. This signifies a zone of convergence. This is further supported by the increase in bed level over this transect in comparison to the seabed directly north and south of the zone, whereby the trough bases decreases in water depth (become shallower) by approximately 1 m over this short section. Bifurcation of the crests are evident in all three timestamps. Furthermore, over this transect, some sediment waves that are asymmetric towards the south-west continue to migrate north-westward until further along the transect where migration direction is in the direction of this new asymmetry direction. This may signify a delay in morphological change or an adaptation to local hydrodynamics.

An alternating convergent and divergent zone pattern continues along the lower slope of the bank and is reflected on the upper slopes closer to the crest, yet at slightly different locations and rates (Figure 9B,C). The most northern convergent zone on the upper slope marks the location of the first of a sequence of five relatively large sediment ridges that extend in a curvilinear form from bank crest to bank base. This curvilinear form correlates with differential migration directions of the sediment wave crests located on the upper slopes compared to lower slopes, i.e., these north-westward migrating waves on the upper slope is met with longer fetched sediment transport pathway earlier (more south) than the part of the same sediment wave crest on the lower slope (denoted by 'F' in Figure 9B). This ultimately leads to the curvilinear form of the ridge. The following ridges do not show such a distinct curvilinear form, yet correspond to a similar orientation change from bank base to bank slope as with Arklow Bank sediment waves.

Lucifer–Blackwater Bank Complex Associated Waves

All derived sediment wave fields north of this site within the Lucifer–Blackwater Bank complex (site 2A, 2B, 2C, and 2F) (Figure 2) display asymmetric, sharp-crested sediment waves (Figure 4) migrating at an average 6.6 m/yr to 10.4 m/yr in a southward direction on the lower slopes of the banks and a distinct increase to 15.7 to 18 m/yr in a

similar direction on the upper slopes (Figure 7). This decrease in migration rate with increasing water depth and distance from the bank crest is distinctly shown in site 2B and 2C as multiple time-lapse bathymetric datasets were analysed, which provided a relatively good spatial extent to allow accurate analysis. Amalgamation process was similarly observed between time-lapse datasets. Whilst 2B and 2C sediment waves are generally simple, waves at site 2A tend towards compound. The orientation of the sediment wave crests at site 2A are heavily linked to the bank topography. At least four distinct orientation changes of the crests are evident that correlate directly with the undulating topography of Blackwater Bank. Nonetheless, although a crest orientation change is detected, sediment wave direction and rate does not seem to be affected.

Long Bank Associated Sediment Waves

The Holden's Bed–Long Bank complex (Figure 1) displays a similar asymmetry to Lucifer Bank, whereby its lee and stoss slope face landward and offshore respectively. However, its shape is quite different, whereby a large rounded form characterises its southern extent, which narrows and tapers as you progress northwards. The southern rounded extent of the bank displays progressive, asymmetric southward migrating sediment waves on both east and west side of the bank at a rate of 31.2 m/yr and 41.2 m/yr respectively (site 3B) (Figure 7). The south-western sediment waves are more rounded, whereas the south-east sediment waves are sharp-crested (Figure 4). As distance increases away from the eastern side of the bank, sediment waves of similar morphology migrate southwards at a decreased rate of 21.3 m/yr (site 3A). Intriguingly, at the southern tip of the bank, sediment waves reverse direction and migrate up on to the bank at a rate of 45.5 m/yr. Furthermore, the upper slopes of the relatively narrow mid to northern section of Long Bank (site 3C) exhibit relatively widely spaced (~150–200 m), sharp-crested, progressive waves migrating in a northward direction at a rate of 23.1 m/yr. Sediment waves closer to the crest of the bank tend towards a symmetrical form, yet the waves slightly downslope are asymmetric.

Evidently, sand bank associated sediment wave morphologies and migration parameters vary immensely over a relatively small distance. The spatio-temporal evolution of these bedforms reveals a highly complex bed load sediment transport regime that divert from the previously understood southward, regional scale sediment transport pathway. Drivers of these patterns is discussed in Section 5.1.

4.2.3. Sediment Waves Independent of Sediment Banks

Site 6

Only two time-lapse bathymetric datasets, of low temporal resolution (approximately 3068 day or 8.4 yr), are available for site 6 (Figure 2). Consequently, only a limited number of sediment waves could be accurately analysed to derive migration parameters. In this context, the highly morphodynamic site can be split into three main sub-regions considering both sediment wave type and migration parameters (see the south-eastern set of sediment waves in Figures 4B and 7B):

- (i) The north-western sector, characterised by very large southward migrating (7.4 m/yr) asymmetric sediment waves;
- (ii) The south-eastern sector, characterised by very large northward migrating (8.2 m/yr) asymmetric sediment waves;
- (iii) The central and southern sector, dominated by very large trochoidal (symmetrical) sediment waves, whereby their complete bedform remains relatively immobile but sediment wave crests and/or upper slopes notably migrate at an average rate of 1.8 m/yr.

The north-eastern sector of the site is characterised by very large, regular, asymmetric, progressive, sharp-crested sediment wave assemblage that migrate south-south-westward at an average rate of 7.4 m/yr. The southern extent of this assemblage is bound by several irregularly spaced very large trochoidal (symmetrical) sediment waves. The crest

of these trochoidal waves seem to migrate north-eastward at an average of 1.8 m/yr, yet their troughs remain immobile. This suggests that (a) flexing of the crest may be occurring or (b) mobilisation of just the upper slopes of these sediment waves, while the bedform unit remains relatively immobile. Spatial resolution discrepancies between the two time-lapse bathymetric datasets were considered an underlying reason for these observations. However, surrounding these very large sediment waves are a limited number of irregular, large, asymmetric sediment waves that migrate in the same north-eastward direction at an average rate of 2.4 m/yr, thus supporting the low mobility characteristics of the upper layer of the trochoidal waves. Deep scour marks are evident at the eastern and western troughs of these trochoidal waves (Figure 5d). This subsequently supports their general immobility, as these bedforms must have been relatively stationary over a relatively long period of time for local hydrodynamics to carve out such significant scour marks, where none are evident on coincident mobile bedforms.

The southern limit of these trochoidal sediment waves are bound by an assemblage of asymmetric, large sediment waves from which migration parameters could not be resolved. South of this assemblage, large trochoidal sediment waves of similar form and migration parameters scatter across the site. Concurrently, at the eastern perimeter of the site, a limited amount of trochoidal waves exhibit an upper slope mobility of 1.3 m/yr in the opposite direction (southwards). This is coincident with an asymmetric, sharp-crested, progressive sediment wave assemblage migrating southwards at an average rate of 5.6 m/yr.

The asymmetric, progressive sediment wave assemblage in the south-western section of the site is of similar shape and size to the north-eastern assemblage, but migrates north-eastward at an average rate of 8.2 m/yr.

Site 5

Site 5 (Figure 2) is dominated by very large, asymmetric, sharp-crested, progressive sediment waves, intermixed with scattered, isolated, very large, trochoidal sediment waves that are encompassed by deep scour marks (Figure 4A; Table 4). These trochoidal waves resemble those identified at site 6. Migration parameters and sediment wave characteristics are derived from two time-lapse bathymetric datasets of time interval 189 days.

Most of the site is characterised by asymmetric, progressive, sharp-crested sediment waves migrating north-eastwards at an average rate of 15.8 m/yr (Figure 7D; Figure 4A). Interrupting this migration pattern are the presence of very large trochoidal sediment waves, whereby the bedform crest migrates or 'flexes' in the same north-eastward direction at approximately 2.5 m/yr (Figure 7D), yet the bedform unit remains immobile. This phenomenon is analogous to site 6 (Figure 2). This northward migration is further locally interrupted in a north-eastern area of the site whereby northward migration is reduced to 7.5 m/yr and is met with large sediment waves migrating in the opposite direction at 17.7 m/yr. This sediment transport convergence zone is marked by a relatively larger sediment wave or ridge. North of this area, sediment waves continue migrating north-eastwards at 18.8 m/yr.

Site 8

The sediment wave assemblages at site 8 markedly combine to form an elongated curvilinear (N–S trending) wave field, extending approximately 16 km long and 2 km wide (Figure 10B). Sediment wave crests orientate approximately NW to SE. At various intervals along the assemblage, sand accretion notably increases along an approximate mid-line/zone, and sediment waves begin to resemble a N to S trending sand ridge. At these sections, transverse bedforms noticeably align with the slope of the ridge. This ridge formation is discontinuous and is integrated with relatively subdued, flat-bedded independent sediment waves (see cross-sections a–e in Figure 10). This study analyses sediment wave characteristics and evolution over time from a 200 × 7000 m survey area of time-lapse bathymetric datasets (Table 2) along the western section of the assemblage, and

a 500 × 3000 m survey area that stretches across the assemblage from west to east in the southern half of the wave field (Figure 10).

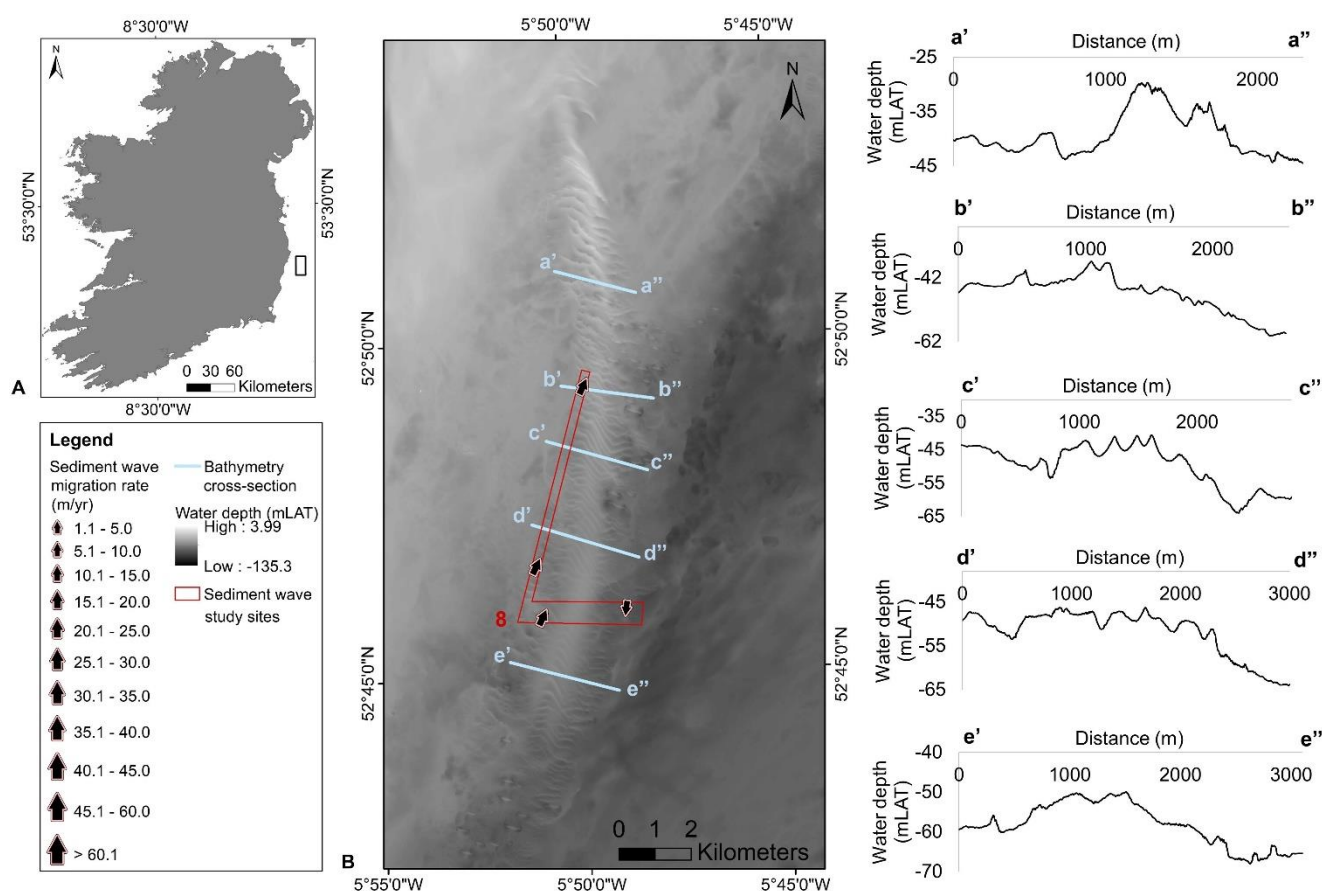


Figure 10. Sediment wave dynamics at offshore independent sediment wave assemblage at site 8 in the Irish Sea. Location of cross-sections a to e are provided in (B). Location of (B) is given in (A). Bathymetry. Source: composite map produced from INFOMAR datasets (<https://www.infomar.ie/data> [Accessed: 10 June 2021]) (see Section 3.1).

From the analysed sections, large to very large, asymmetric, progressive, round-crested sediment waves migrate at an average rate of 16.5 m/yr along the western perimeter of the site over a 7 km distance (Figure 4; Figure 10). Contrastingly, on the eastern side of the ridge, large, asymmetric, round-crested sediment waves migrate southwards at 13.5 m/yr. Sediment wave asymmetry is predominately in the direction of migration. The amalgamation of sediment waves is evident from the time-lapse bathymetry datasets.

Site 7

At site 7 (Figure 2), migration parameters and morphological evolution of sediment waves over time could only be derived from the 2020 and 2021 datasets (except for immobile trochoidal waves) as the time interval between these and the 2012 dataset were too long to derive accurate results.

The south is characterised by large, asymmetric, sharp-crested sediment waves travelling north-eastwards at 12.8 m/yr (south-western set of sand waves in Figures 4B and 7B). This northward migration is locally interrupted by very large sharp-crested trochoidal waves (Figure 5d) that show an overall immobility over the three time-steps yet exhibit a northward movement, or flexing, of 2.9 m/yr at the bedform crest. Scour marks around these isolated bedforms are present, comparable to those at sites 5 and 6. Large sediment waves continue to migrate northwards, gradually reducing in rate from 12.2

m/yr to 9.5 m/yr. These reducing migration rates correlate with the transition into a regular, sharp-crested, very large sediment wave assemblage that progressively changes from asymmetrical towards the north-west, to a symmetrical form, to asymmetrical in the opposite direction (south-eastwards). Towards the northern section of the site, south-eastward facing sediment waves migrate at a rate of 2 m/yr. Clearly, this marks the presence of a convergent sediment transport pathway.

Clearly, sediment wave migration dynamics and morphological changes over time in offshore sediment wave fields vary immensely, both locally within individual sites and between sites, indicating a highly complex bedload sediment transport and hydrodynamic regime. Drivers of these observations and their context in terms of the wider sediment transport regime are discussed in Section 5.

4.3. Comparison between Sand Wave Characteristics, Environmental Parameters and Theory-Based Indicators

4.3.1. Correlation of Individual Sand Wave Characteristics with Environmental Parameters

For the full dataset and for each of the three separate environments, results show a weak to moderate positive correlation [87] between sediment wave height and water depth. However, no association is determined between wavelength and water depth (see supplementary material for statistical correlations). The Sand Wave Index (SWI) (L/H) was adopted from Zhou, et al., [4] in order to understand the impact of water depth on sediment wave shape. A weak to moderate negative power-law relationship was derived from the full dataset and each of the three compiled environments (see supplementary material for full results). This negative correlation suggests the prevalence of more subdued sediment waves (long wavelengths relative to shorter wave heights) in shallow water, and taller, sharper sediment waves (shorter wavelengths relative to higher wave heights) in deeper waters.

No statistically strong relationship can be determined between individual sediment wave dimensions and D_{50} , maximum or mean tidal current velocity or P (Rouse number as in Equation (9)). A decrease in height with increasing residual current magnitude is evident ($H = 1.7U_{c_{res}}^{-0.12}$, $r = 0.114$) yet this correlation is very weak. Statistical correlations are provided in tabular format as supplementary material.

4.3.2. Relationship between the Spatial Distribution of Environmental Parameters/Processes and the Occurrence of Sand Waves

The spatial distribution of P reveals a non-statistical relationship with sediment wave assemblages, whereby increasing P corresponds to a decrease in observed mobile bedforms. Particularly, five distinct regions of relatively higher P are identified. These will henceforth be referred to as 'transition zones' (labelled T1 to T5 in Figure 11). As P is dependent on w_s , this parameter displays a strong positive correlation with increasing grain sizes. The spatial distribution of P across the study area reveals a widespread dominance of bedload transport. Significantly, sediment wave assemblages from both environments tend to occur in regions where $3 < P < 25$ with a median value of 5.7. Outside these zones, relatively higher median P are evident, and correlate well with less mobile, coarser sediments in the transition zones (Figure 11; Figure 1C). As P increases with increasing grain sizes and decreasing flow strength, where P is high, this is attributed to low current velocities relative to high grain sizes.

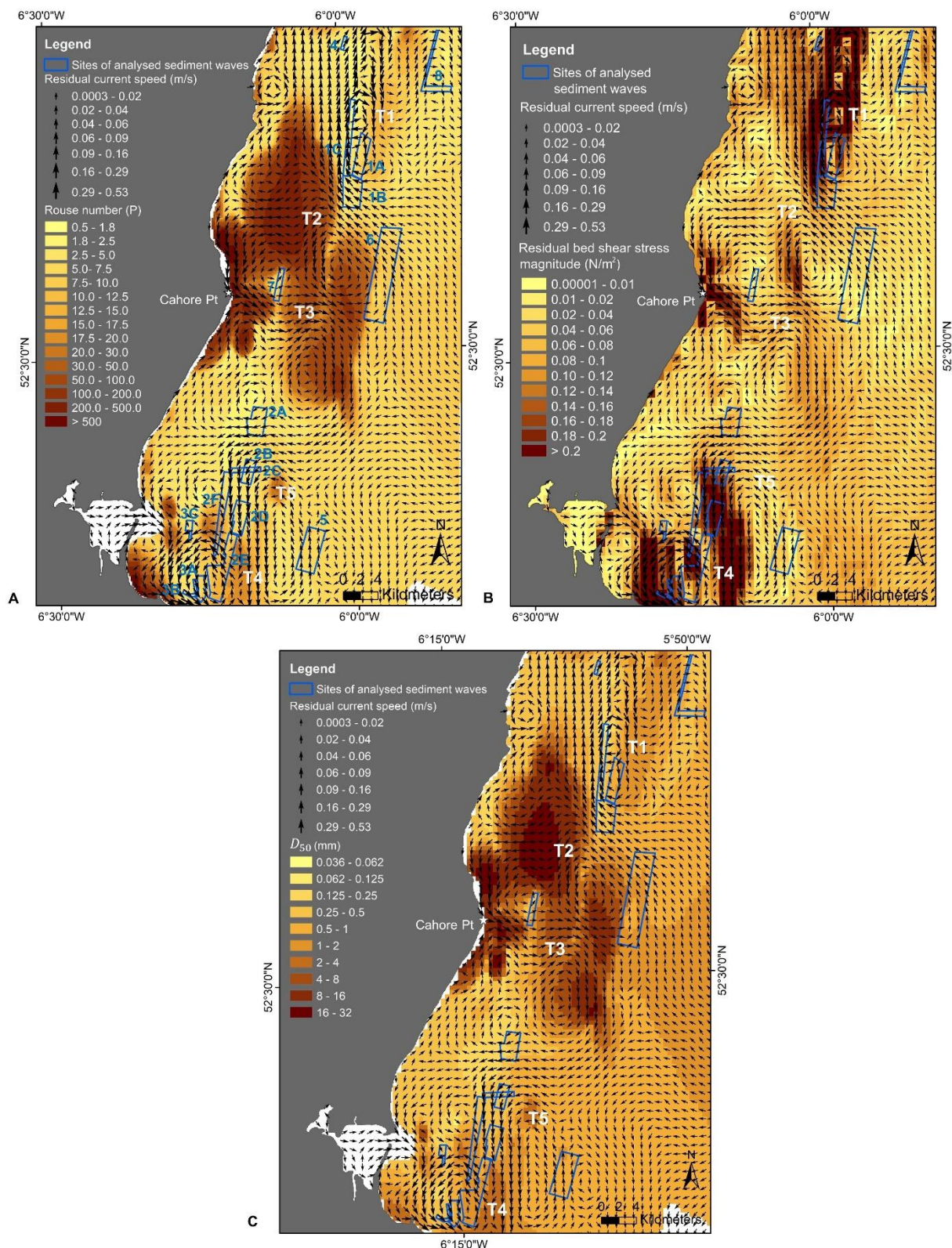


Figure 11. Spatial distribution of (A) dimensionless Rouse number, (B) residual bed shear stress (N/m²) and (C) median grain size (D_{50}) overlain by residual current velocity with location of newly analysed sediment wave assemblages. Transition zones (labelled in white as T1 to T5) refer to areas of relatively higher Rouse number, higher residual current velocity, and coarse grain sizes along a residual transport pathway between offshore sand banks and independent sediment wave assemblages.

A reduction in residual bed shear stress and current magnitudes along a transport pathway corresponds well with the occurrence of independent sediment wave assemblages (Figure 11). All analysed independent sediment wave fields follow this trend. The opposite is found to be true in relation to the transition coarser grained zones (T1 to T5), identified using *P*. Additionally, migration directions generally agree with residual current flow and bed shear stress directions. This will be discussed in Section 5.1.2.

5. Discussion

5.1. Connection between Average Net Sediment Wave Migration Directions and the Wider Sediment Transport Regime in the Irish Sea

Previous bedform- and numerically-derived sediment transport pathways suggest a net southward sediment transport pathway in the southern Irish Sea (Figure 1) [5,26,27,39]. However, the analysis detailed in this study suggests that there is greater complexity to sediment wave behavior, which has subsequent implications for the identification of sediment supply systems involving sediment transfer between various bedform types. In particular, sediment banks exert a significant influence on these patterns. With this new ground-truthing knowledge presented in Section 4, this section aims to elucidate the complex interaction of closed/semi-closed sand bank sediment transport systems and offshore mobile sediment. This investigation combines residual current and bed shear stress datasets calculated by Creane, et al., [5] with newly derived ground-truthing evidence.

5.1.1. Sediment Waves Associated with Sandbanks

The south- and north-ward migrating sediment waves on the east and west sides of Arklow Bank reveal an ebb and flood dominance, respectively. This is due to the slight anticlockwise rotation of Arklow Bank to the principle tidal current axis, leaving the east and west sides of the bank exposed to the ebb and flood tidal phase, respectively [88,89]. Residual tidal current and bed shear stress vectors support these observations (Figure 12). This bi-directional sediment transport on either sides of linear sand banks also agrees with many numerical modelling and field studies [28,35,37]. The relatively higher sediment wave migration rates on the west side of the bank (32.7 m/yr) in comparison to the east side of the bank (23 m/yr) suggest a higher strength in the flood tidal flow.

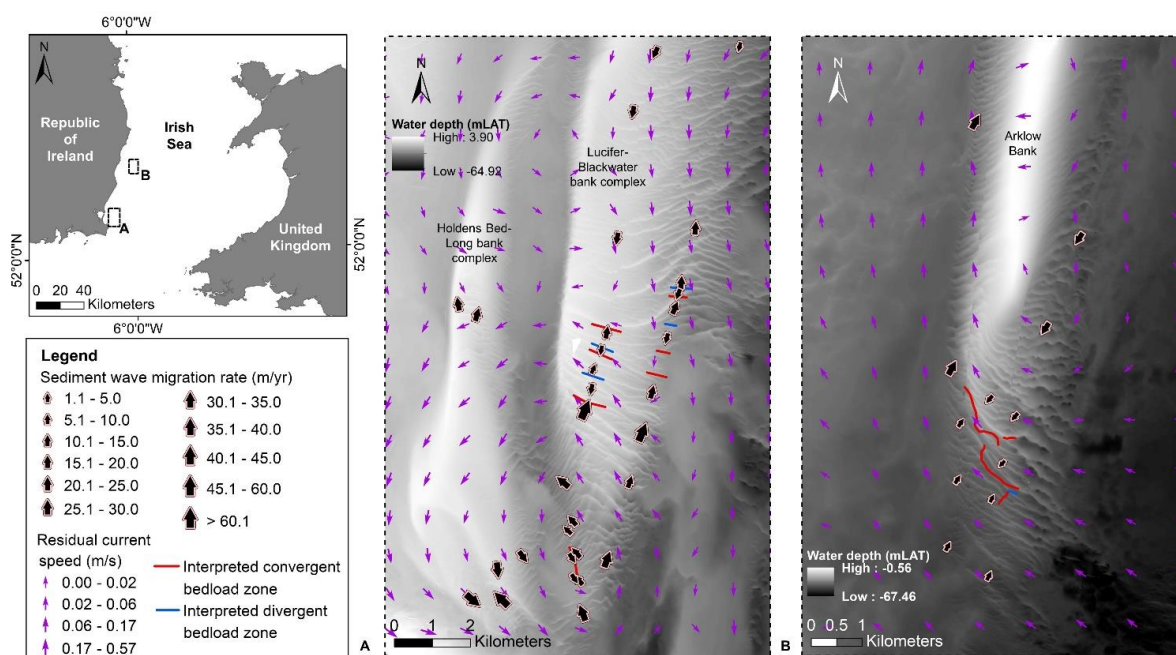


Figure 12. Newly derived sediment wave migration rates and bedload transport divergence and convergence zones overlain by modelled residual tidal current vectors at (A) the southern extent of

Lucifer–Blackwater and Holden’s Bed–Long Bank complexes, and **(B)** the southern half of Arklow Bank in the Irish Sea. Bathymetry source: composite map produced from INFOMAR datasets (<https://www.infomar.ie/data> [Accessed: 10 June 2021]).

Furthermore, a clear semi-closed anticlockwise circulatory sediment transport system is revealed by a of the following observations:

- (i) A convergence zone at the southern end of Arklow Bank, marking the limiting extent of southward migrating sediment waves;
- (ii) Sudden changes in migration rate and morphological character of sediment waves at the intricate pivoting phenomenon at the southern end of the bank (Section 4.2.1);
- (iii) Southward and northward residual flow on the east and west sides of the bank respectively;
- (iv) North-westward flow coming from the south-east of the bank, travelling across the southern extent of the bank and pushing northwards on the western side.

This north-westward flow limits the southern extent of the southward residual flow on the east side of the bank, ultimately driving sediment across the southern extent of the bank and back up along the western side of the bank. This north-westward residual flow propagates over the sediment wave assemblage at site 6 (Figure 2) prior to reaching Arklow Bank (Figure 11) and so has the potential to transport additional sediment into this circulatory system (Section 5.1.2). These provide a hydrodynamic mechanism for an anticlockwise semi-open hydrodynamic and sediment transport regime around Arklow Bank. This supports Johnson, et al., [28] who suggested a circulatory flow system does not necessarily represent a closed-system.

Furthermore, the refraction of tidal flow across the bank is evident at Arklow Bank. Similar observations has been noted at other banks on the European Continental Shelf [90]. This cross-flow aligns well with the progressive orientation change of sand wave crests along the bank slopes, indicating a convergence at the bank crest.

Contrastingly, the Lucifer–Blackwater Bank complex does not display a similar circulatory sediment transport system to Arklow Bank. Instead, sediment wave migration and residual tidal flow reveal a predominately southward net sediment transport pathway along the eastern side of these banks (Figure 6; Figure 12). This is accompanied by a residual anticlockwise current eddy extending from the headland at Greenore Point (Figure 2; Figure 12). This residual eddy ultimately acts as a driving mechanism for the intricate migration characteristics and maintenance of sediment waves at the southern end of Lucifer–Blackwater and Holden’s Bed–Long Bank complexes.

The central zone of this residual gyre (Figure 12A) is characteristic of relatively reduced residual tidal currents and bed shear stresses, and the meeting point of opposing flows. This zone perfectly overlays the 1000 m section of pivoting sediment wave crests located on the south-western side of the Lucifer–Blackwater Bank complex (Figure 9D; Figure 12). Specifically, the progressive south to north-west sediment wave sequence of:

- (i) uni-directional (north-westward) and constant migratory rate along the same wave crest,
- (ii) bi-directional migration along the same wave crests,
- (iii) uni-directional (north-westwards) yet differential rate migration along the same wave crest, and
- (iv) uni-directional (north-westward) and constant rate,

align with the placement of the central zone of this residual gyre. This anticlockwise flow proceeds across Holden’s Bed–Long Bank complex and back towards Greenore Point, driving the southward migration of sediment waves at sites 3A and 3B (Figure 2). On Lucifer Bank, the increased residual current and bed shear stress magnitudes at the outer circumference of the circulatory flow correlate extremely well with significant increases in sediment wave migration rates, i.e., 59.1–72.6 m/yr. Concurrently, the transition zone beyond this point, where a convergence of the residual gyre with the southward transport pathway is revealed, marks the location of the intricate bedload convergence–divergence

sequence outlined in Section 4.2.2 (Figure 12A; Figure 9D). Fundamentally, this circular motion of the residual gyre suggests a continuous recycling of material between Long and Lucifer Banks and associated sediment waves.

The pear-shaped form of the Holden's Bed–Long Bank complex, the nature of sediment wave migration and morphological characteristics, and the presence of this residual eddy provides evidence that the Holden's Bed–Long Bank complex should be categorised as 'Type 3A: headland associated banks—banner bank' [25] as opposed to the neighbouring Lucifer–Blackwater Bank complex and Arklow Bank which are clearly 'Type 1: Open shelf linear sand banks'. Banner banks are described to have been formed and maintained predominantly by headland-generated residual eddies, which trap sediment produced by coastal erosion or arising from seafloor erosion. While many studies suggest these secondary convergent flows generate sand banks at the centre of the residual eddy [25,91,92], further research reveal that the centre of the modelled residual current eddy is not necessarily located over the banner bank but offset at a certain distance [93–95]. Similar results are shown here, whereby the centre of the residual gyre is offset to the east of the bank (Figure 12A). This supports the concept that sediment deposition at the centre of these eddies are not the main element for the formation of banner banks around headlands [95]. Instead, the interaction between tidal current vectors, bed shear stress, and sediment transport pattern through the duration of the tidal cycle governs the development and maintenance of banner banks [95].

5.1.2. Offshore Sediment Wave Assemblages–Sediment Supply System

When analysing residual bed shear stress and current vectors, multiple circulatory cells are revealed that originate from sand banks and propagate towards offshore independent sediment wave assemblages. From here, these residual flows either;

- (a) connect back with sand-bank-associated localised flows, suggesting a potential recycling of sediment between sand banks and offshore sand deposits, or
- (b) connect with circulatory cells over the offshore sediment wave field, from which partial diversions extend out to mobile sediments further offshore. In this way, these relatively closer sediment wave fields act as intermediary transport zones to sediment wave fields in deeper waters.

This provides a potential continuous sediment supply for the maintenance of offshore, independent sediment wave assemblages. Three major circulatory systems are identified:

- (i) The dynamic interaction of the sediment transport regimes at site 7 and site 6 (Figure 13a) with the southern extent of Arklow Bank and the northern extent of the Lucifer–Blackwater Bank complex (Figure 13b);
- (ii) The circulatory residual flow between the eastern edge of Arklow Bank and the sediment wave assemblage at site 8 (Figure 13c);
- (iii) The circulatory cell connecting the Lucifer–Blackwater Bank complex with site 5 (Figure 13d).

The average migratory direction of sediment waves aligns well with the residual transport directions in all three circulatory systems.

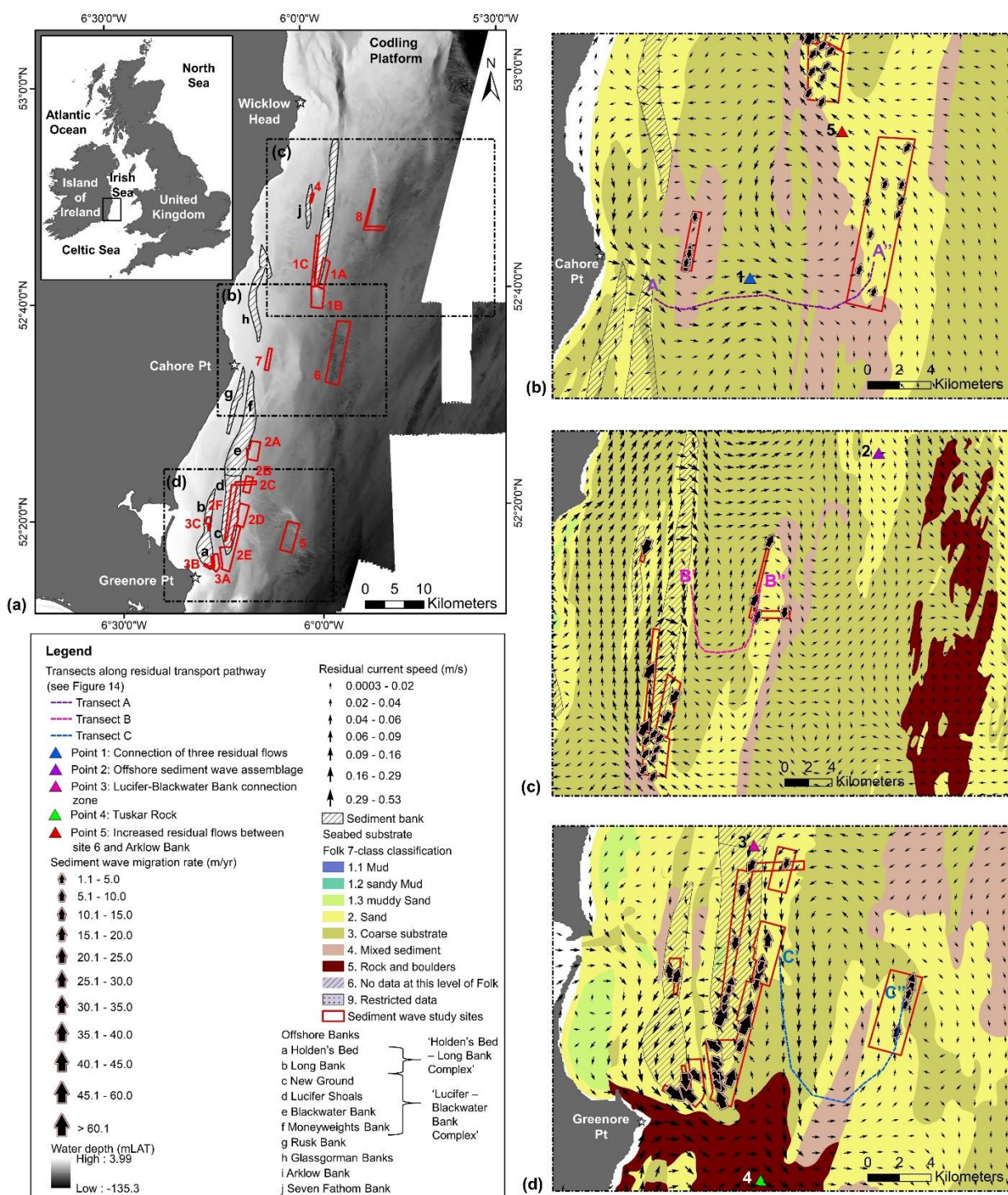


Figure 13. Overview of three residual circulatory transport systems in the south-western Irish Sea connecting offshore sediment banks with independent offshore sediment wave assemblages: (a) Location of three circulatory systems, main offshore sediment banks mentioned in the text and areas of analysed sediment waves by this study, (b) circulatory system (i) outlined in the text (5.1.2), connecting assemblages at site 6 and site 7 with Lucifer–Blackwater Bank complex and Arklow Bank, (c) circulatory system (ii) outlined in the text connecting sediment wave assemblage at site 8 and the further offshore assemblage at Point 2 with Arklow Bank, and (d) circulatory system (iii) outlined in the text, connecting the sediment wave assemblage at site 5 with the Lucifer–Blackwater Bank complex. Transects in A, B, and C are presented in Figure 14. Bathymetry source: composite map produced from INFOMAR datasets (<https://www.infomar.ie/data> [Accessed: 10 June 2021]) (see Section 3.1). Seabed substrate source: EMODnet Seabed Habitats initiative (<http://www.emodnet-seabedhabitats.eu/> [Accessed: 25 June 2021]) [41].

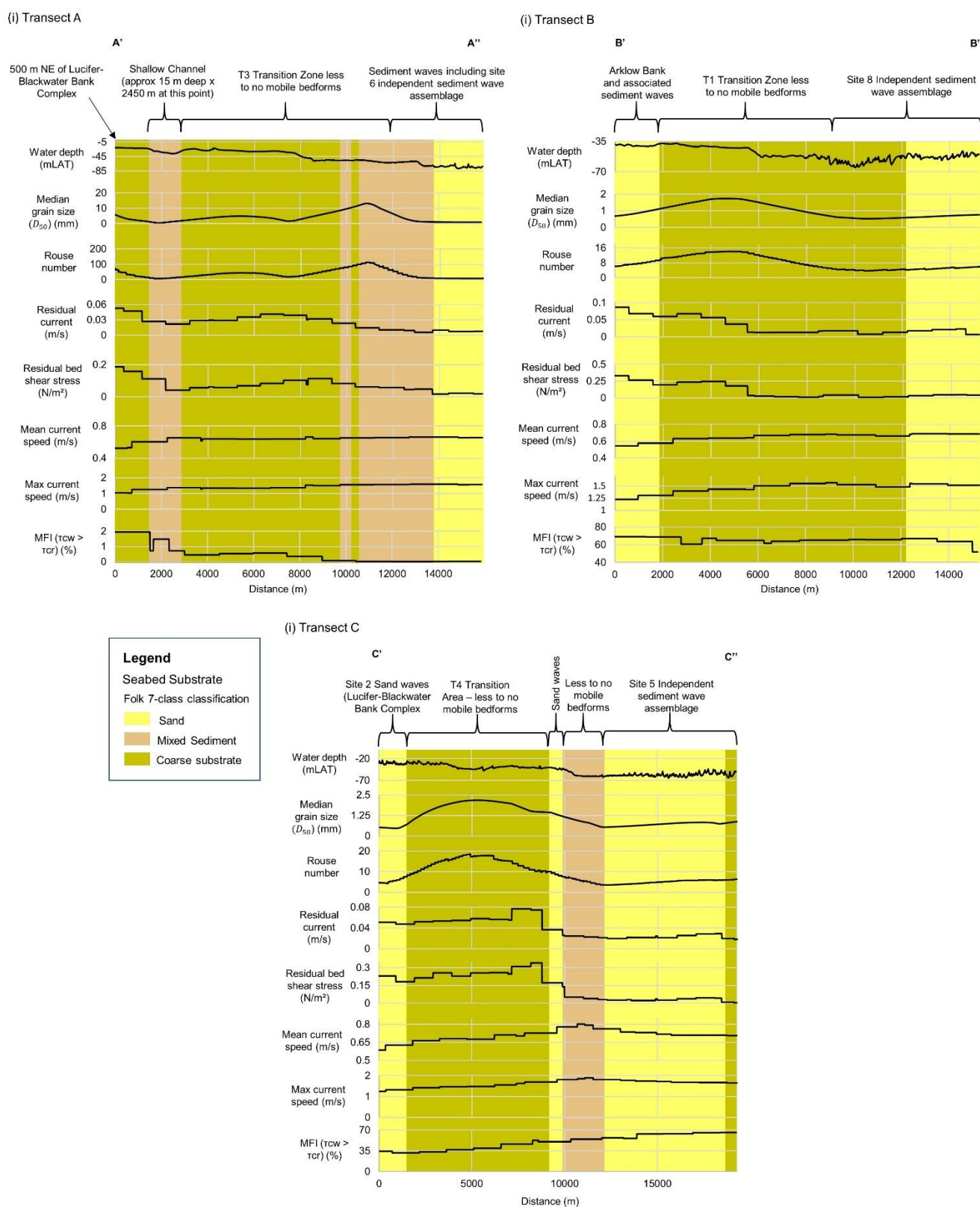


Figure 14. Transects along residual transport pathways in each circulatory system connecting offshore sediment banks with independent offshore sediment wave assemblages. Location of transects are presented in Figure 13. Data used in this Figure is described in Sections 3.3–3.5. Mobilisation Frequency Index (MFI) data source: Coughlan, et al., [64]. Seabed substrate source: EMODnet Seabed Habitats initiative (<http://www.emodnet-seabedhabitats.eu/> [Accessed: 25 June 2021]) [41].

The first circulatory cell originates from the north-eastern region of the Lucifer–Blackwater Bank complex, pushing north-eastward, where it merges with two residual flows (Point 1 in Figure 13b): (i) an eastward flow originating from Cahore Point, and (ii) a southward flow that diverges from the southern tip of Arklow Bank. This integration of three flows marks the point of contact of the outer circumferences of three circulatory flow cells offshore Cahore Point. This merged flow of high magnitude residual current and bed shear stress migrates towards site 6 (Figure 13). A significant reduction in residual magnitudes is evident as the flow approaches site 6, where it is met with residual flows coming from relatively deeper waters to the south-east and east. These combined flows migrate north-westward across site 6, up towards the southern tip of Arklow Bank. Net sediment wave migration direction correlates well with these pathways.

A sudden increase in residual current and bed shear stress directly beyond these progressive asymmetric transverse bedforms is evident, flowing towards the base of Arklow Bank (Point 5 in Figure 13b). This sediment transfer out of the independent sediment wave field acts as an additional sediment supply for Arklow Bank. This flow pattern provides evidence of a high suspended sediment concentration within the north-westward residual flow pathway that has been identified previously by Creane, et al., [5]. This supports the hypothesis that this pathway transfers additional sediment into the dynamic circulatory hydrodynamic and sediment transport cell around Arklow Bank, ultimately defining the system as semi-open [5]. This flow continues northwards into the locally-driven flow around Arklow Bank and diverts southwards in two routes: (i) south-westward towards Cahore Point and (ii) southwards, completing the circulatory cells feeding into site 6.

Furthermore, the centre of the circulatory cell approximately 5 km east of Cahore Point marks an area of highly reduced residual current and bed shear stress magnitudes. This coincides with the newly derived convergent sediment transport pattern at site 7. The high migration rates revealed in the southern section of the site correlate well with high residual magnitudes of the outer circumference of the circulatory field. However, relatively reduced, immobile waves in the north correlate with the centre of the residual cell.

The second circulatory cell connects the eastern side of Arklow Bank with the sediment wave assemblage at site 8, approximately 5.5 km east of Arklow Bank (Figure 13c). A relatively high residual transport pathway moves southward along the eastern edge of Arklow Bank. Part of the flow at the northern half of Arklow Bank diverts eastwards to north-eastwards across the northern section of the offshore site and continues towards the bed load parting zone (Figure 1) [5]. The main flow continues further south along the edge of Arklow Bank, correlating well with southward migrating sediment waves on the east side of the bank. Over the southern half of the bank, the high magnitude flow turns progressively eastwards towards the offshore sediment wave field, progressively reducing in magnitude. The flow progresses northwards, pushing up along the western side of the analysed site, aligning well with the northward migrating sediment waves (~16.5 m/yr) in this area. At the approximate halfway line of the sediment wave assemblage, the residual flow reverses direction once again, continuing southwards, correlating well with the southward migrating sediment waves (~13.5 m/yr) at this site. This residual flow generates a residual circulatory cell over approximately half of the sediment wave assemblage, whereby flow is continuously fed in via the Arklow Bank. Where this indicates a retention of sediment within the sediment wave field, minor pathways are identified exiting the localised area, migrating towards both the offshore sediment wave assemblage located ~11 km north-east of this site (Point 2 in Figure 13c), and the bed load parting zone at Codling Platform (Figure 13a).

Finally, the third circulatory system connects the sediment wave field at site 5 to the Lucifer–Blackwater Bank complex (Figure 13d). A high magnitude southward residual flow begins on the eastern side of the connection between Lucifer and Blackwater Banks (Point 3 in Figure 13d), migrating southwards gradually progressing further away from the banks. At an approximate alignment with the southern end of Long Bank, the flow is

partially merged with a pathway originating from Greenore Point and the western side of Tusker rock (Point 4 in Figure 13d). This marks progressive divergence of the southward flow eastwards then northwards, pushing offshore towards the sediment wave field at site 5. A similar reduction in residual current and bed shear stress magnitude with the occurrence of finer sediments and the sediment wave fields is noted. The northward flow aligns well with the northward-moving progressive asymmetric sediment waves (~15.8 m/yr) in this region. This residual transport pathway continues northwards to the Lucifer–Blackwater Bank connection zone where a circulatory cell is formed. Several immobile, very large trochoidal sediment waves west of site 5 align with the centre of the circulatory cell, which exhibits relatively reduced residuals and converging flow pathways. However, this bedform type in the Irish Sea has also been determined as originating from post-glacial hydrodynamics when sea-levels were lower, tidal currents were stronger, and sediment supply was abundant [39].

Along each of the transport pathways defined above, the transition area between sand banks and the independent sediment wave fields are associated with relatively higher residual bed shear stress and residual current magnitudes. These transition areas are characterised by relatively coarse sediment (mainly sandy gravel to gravelly sand) and are absent of sediment waves. Residual currents notably decrease along the transport pathway at each of the three sites, positively correlating with decreasing grain size, giving rise to sandy sediments where sand wave assemblages occur independently offshore.

These relatively higher residual currents in the transitional gravelly dominated areas represent a scoured seabed whereby critical bed shear stress is exceeded above a certain threshold so that fine to medium sediment grains (silt and fine to medium sands [96]) are lifted into suspension and transported as suspended load. This causes a winnowing of finer material out of the region. While numerically modelled mean and max current velocities do not display higher magnitudes over these coarser transitional areas in comparison to the offshore sediment wave fields, relatively higher residual current and residual bed shear stress magnitudes are exhibited (Figure 11; Figure 14). This indicates that the residual flow parameters, which correspond to tidal asymmetry, may play a greater role in these circulatory feedback systems in comparison to the strength of the mean or max peak currents. Higher residual currents and bed shear stresses indicate a higher asymmetry in the transport system, therefore high residual currents provide a mechanism for more sediment to be transported out of and/or bypass the region as suspended load in comparison to a symmetrical system. This suggests that sediment originating from the sand banks, at the beginning of each transport pathway, may be transported as suspended load, remaining entrained in the water column, bypassing these transitional zones, until residual current and bed shear stress magnitudes (thus tidal asymmetry) is reduced. The reduction in tidal asymmetry allows sediment to settle out of suspension [97]. This reduction correlates well with the occurrence of independent sediment wave fields in the south-western Irish Sea (Figure 13; Figure 14).

A high bed level change is not expected in these areas as shear stresses exerted on the seafloor are not high enough to readily exceed critical bed shear stress for mobilisation of relatively coarse grain sizes. Furthermore, according to Neill and Couch [97] higher tidal asymmetry zones theoretically display a lower bed level change in comparison to maximum bed level changes at tidal symmetry zones. This is supported by the mobility frequency index (MFI) produced by Coughlan, et al., [64] whereby in each of these transitional zones, the critical bed shear stress is exceeded less frequently by both (a) tidal current- and (b) combined tidal current- and wave-induced bed shear stress, in comparison to sediment wave field zones.

The occurrence and absence of mobile bedforms along a transect at each circulatory system also aligns very well with the theoretical predictor of bed forms defined by Shields [86]. A plot of calculated entrainment function (F_s) against the shear Reynold's number (Re_*) (under mean and maximum depth-averaged current velocities) along each transect is displayed in Figure 15, where 'ripples' refer to transverse bedforms with $L < 0.6 m$. It

is clearly shown that under mean current velocities, sediments do not meet the threshold of motion criteria in the transitional zones; therefore no mobile bedforms are present. Contrastingly, the plot predicts mobile bedforms further along the transport pathway in the independent sediment wave fields at site 5 and 8. Under mean current velocities, the threshold of motion in site 6 is not exceeded, and yet under maximum current velocities sediments are mobilised in this localised area. As expected, under maximum current velocities, the threshold of motion is exceeded more readily for all three transport pathways.

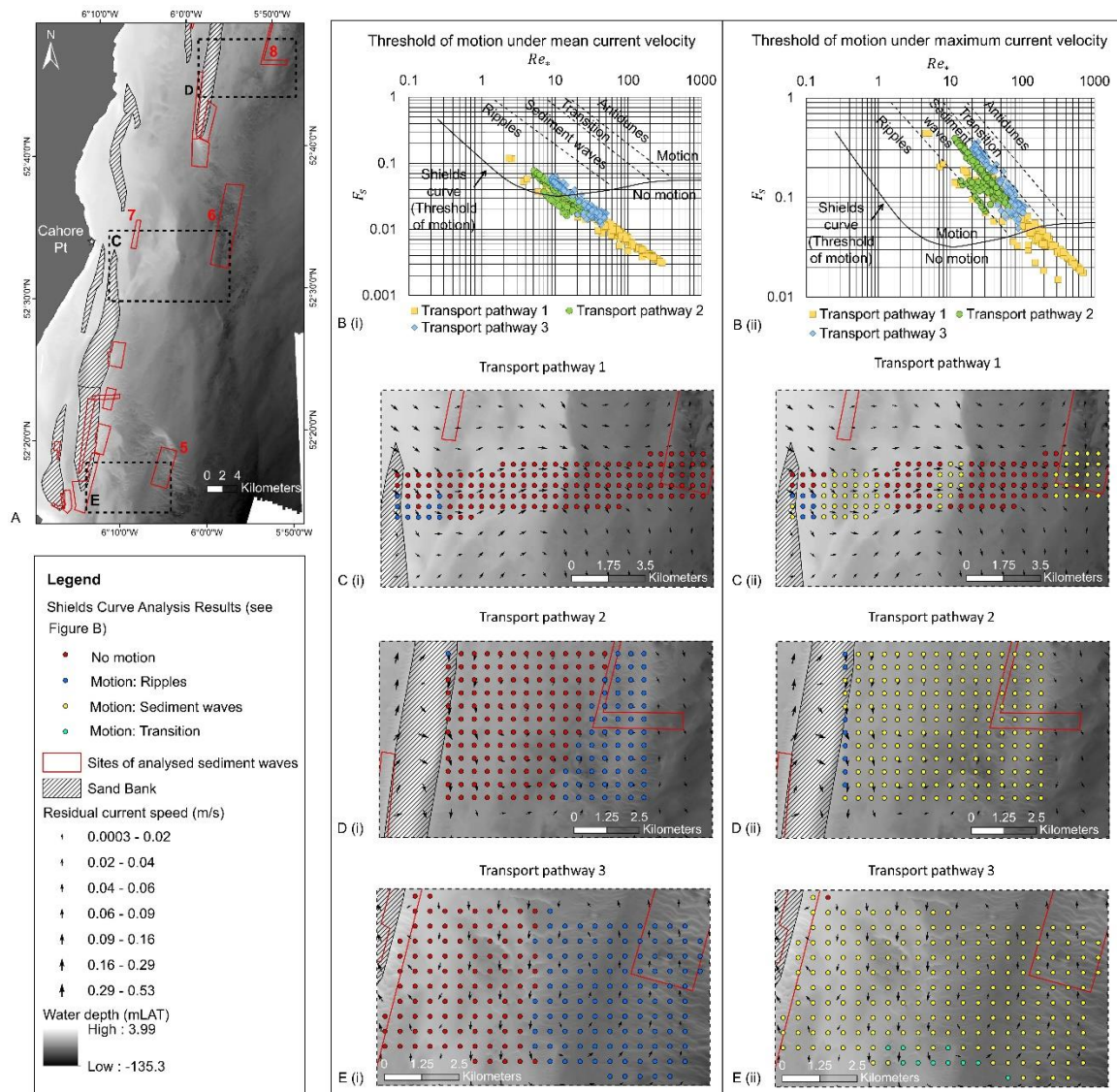


Figure 15. (A) The location of (C–E) in the south-western Irish Sea. (B*i*,B*ii*): The Shields curve [86] overlain with values of Re_* and F_* derived from the sediment surface samples calculated under mean and maximum current velocities, respectively. Sampling locations are displayed in C to E, which form a 500×500 m grid that transects along residual circulatory cell systems 1, 2, and 3 outlined in Figure 13. From (B*i*,B*ii*), each point is designated as (a) No motion or (b) Motion: Ripples, Sediment waves or Transition, the location of which are displayed in (C–E). Bathymetry source: INFOMAR (<https://www.infomar.ie/data> [Accessed: 10 June 2021])

To investigate the mode of sediment transport within these circulatory systems, the spatial distribution of the dimensionless Rouse number (P) was analysed (Figure 11; Figure 14). Previous studies [45,60] found a strong correlation between P and the prevalence of sand wave fields. Specifically, Damen, et al., [45] found that dominant bedload transport ($P > 2.5$) aligns very well with sand wave field boundaries. Although dominant

bed load transport extends beyond the sand wave field boundaries, no sand wave assemblages are found in areas dominated by suspended load transport ($0.8 < P < 1.2$). Subsequently, the Rouse number is incorporated into this study as it has the potential to elucidate the hypothesised circulatory transport systems connecting sand banks and associated sediment waves to independent sediment wave fields.

Each stage of the three circulatory systems displays $P > 2.5$, indicating a dominant bedload transport regime (Figure 11). Furthermore, transition zones clearly display a distinctive relative increase in P in comparison to the location of sediment wave fields and sand banks (Figure 14). This contrasts to what was found by Borsje, et al., [60] and Damen, et al., [45]. Although sediment wave fields, too, correlated with the bedload transport mode, outside of these areas they were dominated by suspended load. Additionally, a dampening mechanism to sediment wave growth was attributed to suspension of material at the sediment wave crests. Discrepancies between the studies can be explained by the difference in sediment grain sizes between the two previous studies and this study. The seabed in earlier studies is dominated by grain sizes (D_{50}) ranging from 0.1 to 0.5 mm, yet the south-western Irish Sea displays a wide range of sediment types varying from 0.5 to 30 mm (Section 3.3). While dominant suspended load transport, in areas outside sediment wave fields, were attributed to the fine grain sizes characterising the seabed in Damen, et al., [45], relatively coarser sediment characterises the seabed in the transition zones in this study. As P is dependent on the particle settling velocity of a grain, there is a distinct positive correlation between P and grain size (P increases with increasing grain size). Subsequently, Rouse numbers are only representative of sediment at the seabed and do not consider sediment already in suspension, i.e., sediment sourced from sand banks and bypassing the 'transitional' areas as suspended load. Therefore, P in this case does not account for the mode of transport in these circulatory cell systems. A transect along all three transport pathways summarises these findings (Figure 14). The MFI dataset, produced by Coughlan, et al., [64], is less accurate for Transect A compared to B and C (Figure 14) due to the lack of available sediment samples for site 6 in the grain size dataset used by Coughlan, et al., [64]. As a result, the grain size dataset used for MFI calculations shows a higher D_{50} value than what is present at the seabed, subsequently a lower MFI than reality is returned. However, a larger number of sediment samples were compiled for this study (see Section 3.3), therefore median grain size and Rouse numbers (Figures 13 and 14) calculated by this study have a relatively higher accuracy.

5.2. Local Variations in Sand Wave Morphology

5.2.1. Singular Environmental Parameters as an Unreliable Indicator for Sediment Wave Growth

Quantifying the role of individual environmental parameters on sediment wave growth and development is difficult and ultimately proven inconclusive in a number of studies (Section 1.1.2). The limited very weak to moderate relationships derived from this study (Section 4.3.1) reinforce the deficiency of robust derivatives from statistical correlations between singular environmental parameters and sediment wave growth. Ultimately, the different sediment wave morphological variations are most likely driven by a combination of physical processes, therefore the use of singular environmental parameters to understand these bedform dynamics should be made redundant. Instead, a coupled or process-driven approach should be incorporated in future studies.

Results given in Section 4.3.1 coincide with inconclusive findings of several studies outlined in Section 1.1.2. For example, this study found a similar strength yet opposite sign correlation (moderate; $r = 0.42$ – 0.43) between SWI and water depth to sediment waves on the Taiwan Banks [4]. This implies that sand wave shape is more elongated and smaller in relatively shallow water (subdued) and shorter and taller in deeper waters, opposite to that found on the Taiwan Banks. However, although both studies are influenced by locally-driven environmental conditions, both correlations are not statistically strong, have

a large scatter of data points, and do not incorporate other potential control factors such as grain size, tidal current velocity, and mode of sediment transport. Consequently, singular relationships such as these are considered inadequate for a robust interpretation.

Alternatively, analysis of the spatial distribution of sediment waves with process-based parameters such as Rouse numbers, to indicate the dominant mode of sediment transport and residual parameters such as tidal current and bed shear stress, show promise (Figure 11). The mode of sediment transport has shown to be highly useful in understanding sediment wave growth by previous studies [45,60]. Although these studies show that increasing suspended load dominance over bedload transport has a dampening effect on sediment wave heights [45,60], this study does not resolve the same finding, most likely due to a difference in the range of in situ grain sizes (Section 5.1.2). However, a clear correlation is still evident whereby sediment waves occur where $P > 2.5$ (bed load transport dominance), with a median value of $P = 5.7$, and tend to be absent in transitional zones where P is relatively increased ($\sim P > 8$). Therefore, increasing P above a certain threshold may indicate winnowing of sediment from the seafloor, subsequently dampening sediment wave growth and development. Combining this with previous knowledge, this indicates that sediment wave assemblages may only occur within a limited range of P , whereby:

- (a) increasing suspended load dominance ($0.8 < P < 1.2$) over bed load dominance dampens sediment wave growth, and
- (b) increasing bed load dominance ($P > 2.5$) above approximately $P > 8$ (Figure 11) indicates winnowing of finer sediment from the seafloor, leading to sediment starvation and subsequently also inhibiting sediment wave growth.

Similarly, a clear correlation between the reduction in residual tidal current and bed shear stress along a transport pathway with the occurrence of independent offshore sediment wave assemblages (Figure 11; Figure 12) suggests that asymmetry of the tide could be considered a sediment wave growth mechanism. According to Neill and Couch [97], where maximum tidal asymmetry ($2\phi_{M_2} = \phi_{M_4}$, where ϕ is the phase of the tidal constituent noted in its subscript) and maximum bed shear stress occurs, low bed level change is expected. Contrastingly, as tidal asymmetry progresses towards a symmetrical tide ($2\phi_{M_2} = \phi_{M_4} + 90^\circ$), bed level change theoretically increases, thus coinciding with increased sediment deposition or erosion. Similarly, a reduction in tidal asymmetry (lower residual bed shear stress and tidal current velocity) corresponds to a lower level of tide-averaged net sediment transport movement out of a region in comparison to high tidal asymmetry (relatively higher residual currents). Subsequently, a reduction in residual current along a transport pathway not only supplies sediment to these independent offshore sediment wave assemblages (Section 5.1.2) but also indicates a relatively higher retention of sediment in the local area, potentially allowing the growth of sediment wave heights. Clearly, multiple parameters and processes interlink to form a highly complex hydrodynamic system resulting in an intricate morphodynamic and sediment transport regime.

5.2.2. Geological History of the Irish Sea as a Required Background Knowledge for Present Day Sediment Wave Dynamics

In this region, the geological history of the Irish Sea must be considered when interpreting bedform origin, growth, and evolution. Changes in tidal current velocities [98], relative sea level, and an abundant sediment supply during post-glacial marine transgression provide an adequate hydrodynamic and sediment regime for submarine bedform (e.g., sediment bank and sediment wave) formation [5]. Specifically, detailed geophysical analysis and paleo-tidal modelling by Van Landeghem, et al., [39] suggests very large trochoidal sediment waves in the Irish Sea could not have grown to such large heights under present day hydrodynamics. Instead, these most likely formed during post-glacial dynamics at approximately 7–10 ka BP, when relative sea levels were lower, and tide- and wave-driven current velocities were higher. Subsequent bed shear stress reductions are suggested to have made these sediment waves immobile after 5 ka BP, when hydrody-

dynamic conditions stabilised. These trochoidal waves are dominated by coarse-grained material with a thin veneer of fine-grained sediment on the crest and upper slopes. These thin veneers of finer sediments are thought to be active under present day conditions, altering the shape of the slope and crests over time, without shifting the base of the bedform. Scour occurs around the margins of these very large sediment waves due to intensified vortices around its edges, ultimately supplying fine sediment that migrates over the central part of these coarse-grained bedforms. These observations by Van Landeghem, et al., [39] correlate very well with very large trochoidal waves associated at sites 5, 6, and 7. Finer sediments at the slopes and crests of the bedforms tend to migrate under present day hydrodynamic conditions whilst the core bedform remains immobile.

5.2.3. Wave-Influence on Sediment Wave Dynamics

Analysis of time-lapse bathymetric datasets have also revealed (a) a reduction in wave height (b) a change from simple to compound waves, (c) counter-current migration, (d) reverse-asymmetry migration, and (e) sand-bank-associated waves displaying higher migration rates in comparison to independent sediment wave assemblages (Section 4.2.2).

Observations (a) and (b) are most significant over the 169-day period at the Lucifer–Blackwater Bank complex. According to Coughlan, et al., [64] these banks experience a mixed dominance of tide- and wave-induced bed shear stress. The complex tide–wind interaction can specifically have a large impact on residual sediment transport pathways [99], whereby in regions of low tidal amplitude, even moderate wind speeds can reverse residual tidal flows [100,101]. Similarly, numerical modelling works reveal that the interaction between storm waves and tidal currents not only increase bed shear stresses on sand banks, resulting in net erosion and sediment transport, but further influence the direction of net sediment transport associated with these bedforms [102–104]. Mitchell, et al., [104] found that on a tidal sand ridge in the Bristol Channel, sand transport is likely enhanced by surface waves during slack water by maintaining particles above the threshold of motion and providing a bed stress vector in the direction of wave propagation. Although Damen, et al., [45] showed only a weak correlation between Shield’s parameter and sediment wave heights, many studies have shown a high influence of storm waves dampening sediment wave height and generating a more subdued bedform [59].

Sand bank associated sediment waves analysed in this study occur at a maximum water depth of 30 mLAT. For a wave to reach the seafloor at this water depth or shallower, the wave period needs to be at least 6.2 s (s). In situ wave data from the M5 weather buoy, located off the south coast of Ireland (51.690425, –6.704336), was analysed for the 169-day time period. The wave period readily exceeded this 6.2 s threshold. Furthermore, at least four storm events were recorded where the wave period reached 8 s, significant wave heights reached greater than 6 m, and maximum wave heights were greater than 10 m, some reaching 16.4 m. During these storms, the base of the wave could reach the seafloor at water depths less than 50 mLAT, thus implying wave action could easily influence these sediment waves over this time period. The occurrence of these storm waves enhances shear stress exerted on the seabed, causing increased erosion, sediment stirring, and flattening of sediment waves, partially distributing local sediment through relatively smaller superimposed sediment waves (shifting the wave from simple to compound). Over time, tidal currents are predicted to transform these sediment waves back to their original sharp-crested, simple, asymmetric form.

Migration rates of sand-bank-associated sediment waves are notably higher than bedforms in independent assemblages. Two main physical drivers for this may be:

(a) the lower residual tidal current (tidal symmetry/bi-directional flow) at offshore assemblages in comparison to higher residual tidal flow (tidal asymmetry/uni-directional flow) at sand bank associated assemblages, and

(b) pure tide-induced bed shear stress at offshore sediment wave fields in comparison to combined tide- and wave-induced bed shear stress at sand-bank-associated sediment wave fields [64].

Under combined tide- and wave-induced bed shear stress, a higher volume of material is mobilised and potentially transported by the tidal current due to increased stirring by wave action, consequently increasing bedform migration rate [104,105].

Furthermore, in complex hydrodynamic areas such as at bedload convergent zones (e.g., site 7) or at the southern extents of sediment banks (e.g., sites 2E, 2D, and 1C), counter-current and reverse-asymmetry migration is evident. These observations support the findings of Van Landeghem, et al., [30] and further falsify the theory that the migration of sediment waves is predominately in the direction of their asymmetry.

6. Conclusions

Targeted repeat high-resolution bathymetry data from the Irish Sea reveals large to very large sediment waves, of varying morphology, with mean wave heights of 0.6 to 6.1 m. These sediment waves exhibit migration rates of 1.1 to 79 m/yr. Sediment wave characteristics were quantified and compared with similar data from previous studies, significantly augmenting the global dataset. Modelled output for bed shear stress magnitude and direction, as well as other environmental parameters and theoretical indicators, were compared with these sediment wave characteristics to determine influencing factors on sediment wave development and migration. The dataset and results provide valuable insights into the spatio-temporal evolution of sediment waves over a large area of a tidally-dominated shelf sea that is geologically complex in terms of morphology and sedimentology.

Individual environmental parameters were found to be unreliable indicators for sediment wave growth. By contrast, the mode of sediment transport is identified as a controlling factor on sediment wave growth and development. It is suggested that sediment waves are restricted to areas where $\sim 2.5 < P > \sim 8$ for two reasons: a) suspended load dominance over bed load dominance $0.8 < P < 1.2$ dampens sediment wave growth, and b) increasing bed load dominance above $P > \sim 8$ indicates winnowing of finer sediment from the seafloor, leading to sediment starvation and subsequent dampening of sediment wave growth. Residual tidal current and residual bed shear stress is also a suggested controlling factor for sediment wave growth. The reduction in residual tidal current along a transport pathway supplies sediment to sediment waves, thus facilitating bedform growth, by allowing the settlement of sediment out of suspension, and by retaining sediment within the assemblage due to the associated lower level of tide-averaged net sediment transport movement out of a region in comparison to high tidal asymmetry. In addition, the theoretical predictor of bedforms defined by Shields [86], plotting the entrainment function against the shear Reynold's number, aligns well with the occurrence and absence of mobile bedforms in this region. Therefore, this theoretical predictor has the potential to predict seabed mobility and bedform type in other tidally-dominated shelves, and therefore a coupled or process-driven approach (e.g., Rouse numbers) to understanding bedform dynamics should be incorporated in future studies.

The dataset also allowed for the study of sand bank morphodynamics and the interaction between offshore sand banks, associated sediment waves and independent sediment wave assemblages. A key finding of this study is that the net sediment transport pathways in the south-western Irish Sea derived in this study falsify the previously thought consistent southward flow. Divergence from this pattern is clearly seen both at offshore sand banks and at independent offshore sediment wave assemblages, and a number of key observations can be drawn:

1. Arklow Bank contains a semi-closed circulatory hydrodynamic and sediment transport system.
2. Lucifer–Blackwater Bank complex's sediment transport and morphodynamic regime does not show a similar circulatory pattern to Arklow Bank. Instead, a predominant southward transport pathway dominates the eastern slope of the bank complex, and a residual headland eddy heavily influences the southern section of the bank. This residual eddy is most likely a controlling factor for the formation and maintenance of the adjacent banner bank (Holden's Bed-Long Bank complex).

The offset of the centre of this residual gyre to the east of the banner bank supports the concept that sediment deposition at the centre of these eddies are not the main element for the formation of banner banks.

3. The circulatory residual flow between the Lucifer–Blackwater and the Holden’s Bed–Long Bank complexes, combined with newly derived sediment wave migration and morphodynamic patterns, suggests a continuous recycling of material between these two bank complexes and associated sediment waves.

4. Offshore independent sediment wave fields are supported through circulatory residual tidal current cells, originating from offshore linear sand banks. From this, two new phenomena are suggested: (a) a potential recycling of sediment between sand banks and offshore sand deposits, and (b) offshore independent sediment wave fields act as intermediary transport zones to sediment wave fields in deeper waters.

Observations from this study show that the rate of sediment wave migration and morphological change varies hugely both regionally in a tidal dominant shelf, and within individual study sites, depending on local environmental factors including residual tidal current, mode of sediment transport, and wave influence. It underpins the necessity for investigating further the complex interaction between flow and seafloor bedforms, including the need for higher-resolution temporal datasets to qualify bed-level change over short time periods and the value of numerical modelling of bed stress magnitude and direction at a local level. This new information concerning sediment wave dimensions, migration parameters, and the nature of morphological change, can be used not only to optimise infrastructural design but also optimise the monitoring strategy and monitoring frequency for navigation channels, pipelines, cables and turbine foundations, and are highly valuable to the development of more robust marine spatial planning.

Supplementary Materials: The following supporting information can be downloaded at: <https://www.mdpi.com/article/10.3390/geosciences12120431/s1>, Supplementary Material S1: Methodology – sediment wave crest delineation and migration direction and rates, Supplementary Material S2: Results – statistical correlation between sediment wave dimensions and individual environmental parameters, Table S1: Interpretation of Pearson correlation coefficient (r), Table S2: Relationship between sediment wave heights (H) and wavelengths (L) in the south-western Irish Sea. The Full dataset has been broken into three environments i.e. Southern Banks, Northern Banks and Independent Assemblages, and each individual study site, Table S3: Relationship between sediment wave heights (H), wavelengths (L), and Sand Wave Index (SWI) with Rouse Number (P) in the south-western Irish Sea, Table S4: Relationship between sediment wave heights (H), wavelengths (L), and Sand Wave Index (SWI) with Water depth (D) in the south-western Irish Sea, Table S5: Relationship between sediment wave heights (H), wavelengths (L), and Sand Wave Index (SWI) with median grain size (D_{50}) in the south-western Irish Sea, Table S6: Relationship between sediment wave heights (H), wavelengths (L), and Sand Wave Index (SWI) with maximum current speed ($U_{c_{max}}$) in the south-western Irish Sea, Table S7: Relationship between sediment wave heights (H), wavelengths (L), and Sand Wave Index (SWI) with residual current speed ($U_{c_{res}}$) in the south-western Irish Sea, Table S8: Relationship between sediment wave heights (H), wavelengths (L), and Sand Wave Index (SWI) with mean current speed ($U_{c_{mean}}$) in the south-western Irish Sea.

Author Contributions: S.C.: conceptualization, methodology, investigation, formal analysis, writing—original draft, writing—review and editing, visualisation, validation. M.C.: supervision, conceptualization, writing—review and editing. M.O.: supervision, writing—review and editing. J.M.: supervision, conceptualization, writing—review and editing. All authors have read and agreed to the published version of the manuscript.

Funding: S.C. is funded by the Irish Research Council (IRC) through grant EBPPG/2019/158 (Employment-Based Postgraduate Programme Scholarship). M.C. is funded under an Irish Research Council Enterprise Partnership Scheme Postdoctoral Fellowship (EPSPD/2020/109) and in part by a research grant from Science Foundation Ireland (SFI) under Grant Number 13/RC/2092, with support from Gavin and Doherty Geosolutions Ltd. and the Geological Survey of Ireland (GSI). This project benefited from funded industry-academic collaboration involving Gavin and Doherty Geosolutions, University College Dublin (iCrag) and University College Cork (MaREI), supported by the Marine Institute under the Marine Research Programme 2014–2020 (Grant-Aid Agreement No. IND/18/18). Ship time

on the RV Celtic Voyager was funded by the Marine Institute through the 2020–2021 ship-time programme under the National Marine Research and Innovation Strategy 2017–2021.

Data Availability Statement: The bathymetry data used in Figures 2, 4, 7–10, and Figures 12–15, and Figure 1 is sourced from INFOMAR (<https://www.infomar.ie/data> [Accessed: 10 June 2021]) and EMODnet Bathymetry Consortium (2020). Seabed substrate data used in Figures 1, 13, and 14 come from EMODnet Seabed Habitats initiative (<http://www.emodnet-seabedhabitats.eu/> [Accessed: 25 June 2021]). The set-up and validation of the numerical model described in Section 3.4 has been published in a previous paper [57]. Supplementary methodology and results outlined in Sections 3.2.2 and 4.3.1, respectively, are provided as Supplementary Material to this paper.

Acknowledgments: The authors would gratefully like to acknowledge the Mobility of Sediment Waves and Sand Banks in the Irish Sea (MOVE) (CV20010, CV20036 and CV21035) shipboard crew and scientists, and onshore Marine Institute and INFOMAR support personnel for assistance with data acquisition. The authors are appreciative for access to the seabed sediment sample data and would like to acknowledge colleagues collecting and preparing these data through the projects and surveys mentioned. The authors wish to thank Xavier Monteys and Charise McKeon (both GSI) in particular for aiding with the INFOMAR dataset. Seabed substrate information contained here has been derived from data that is made available under the European Marine Observation Data Network (EMODnet) Seabed Habitats initiative (<http://www.emodnet-seabedhabitats.eu/> [Accessed: 25 June 2021]), financed by the European Union under Regulation (EU) No 508/2014 of the European Parliament and of the Council of 15 May 2014 on the European Maritime and Fisheries Fund.

Conflicts of Interest: The authors declare no conflict of interest.

References

- Gamberi, F.; della Valle, G.; Marani, M.; Mercorella, A.; di Stefano, S.; di Stefano, A. Tectonic Controls on Sedimentary system along the Continental Slope of the central and southeastern Tyrrhenian Sea. *Ital. J. Geosci.* **2019**, *138*, 317–332. <https://doi.org/10.3301/IJG.2019.08>.
- Short, A.D. Sediment transport around Australia—Sources, mechanisms, rates, and barrier forms. *J. Coast. Res.* **2010**, *26*, 395–402. <https://doi.org/10.2112/08-1120.1>.
- Zhou, J.; Wu, Z.; Zhao, D.; Guan, W.; Cao, Z.; Wang, M. Effect of topographic background on sand wave migration on the eastern Taiwan Banks. *Geomorphology* **2022**, *398*, 108030. <https://doi.org/10.1016/j.geomorph.2021.108030>.
- Zhou, J.; Wu, Z.; Zhao, D.; Guan, W.; Zhu, C.; Flemming, B. Giant sand waves on the Taiwan Banks, southern Taiwan Strait: Distribution, morphometric relationships, and hydrologic influence factors in a tide-dominated environment. *Mar. Geol.* **2020**, *427*, 106238. <https://doi.org/10.1016/j.margeo.2020.106238>.
- Creane, S.; O’Shea, M.; Coughlan, M.; Murphy, J. The Irish Sea bed load parting zone: Is it a mid-sea hydrodynamic phenomenon or a geological theoretical concept? *Estuar. Coast. Shelf Sci.* **2021**, *263*, 107651. <https://doi.org/10.1016/j.ecss.2021.107651>.
- Galvez, D.S.; Papenmeier, S.; Sander, L.; Bartholomä, A.; Wiltshire, K.H. Ensemble mapping as an alternative to baseline seafloor sediment mapping and monitoring. *Geo-Mar. Lett.* **2022**, *42*, 1–13. <https://doi.org/10.1007/s00367-022-00734-x>.
- Auguste, C.; Marsh, P.; Nader, J.R.; Penesis, I.; Cossu, R. Modelling morphological changes and migration of large sand waves in a very energetic tidal environment: Banks Strait, Australia. *Energies* **2021**, *14*, 3943. <https://doi.org/10.3390/en14133943>.
- Szczuciński, W.; Jagodziński, R.; Hanebuth, T.J.J.; Statterger, K.; Wetzel, A.; Mitrega, M.; Unverricht, D.; van Phach, P. Modern sedimentation and sediment dispersal pattern on the continental shelf off the Mekong River delta, South China Sea. *Glob. Planet. Change* **2013**, *110*, 195–213. <https://doi.org/10.1016/j.gloplacha.2013.08.019>.
- Robinson, K.A.; Ramsay, K.; Lindenbaum, C.; Frost, N.; Moore, J.; Petrey, D.; Darbyshire, T. *Habitat Mapp. Conserv. Manag. South. Ir. Sea (HABMAP). II Model. Mapp.* **2009**, *5*, 210.
- Wilson, B.R.; Brown, C.J.; Sameoto, J.A.; Lacharité, M.; Redden, A.M.; Gazzola, V. Mapping seafloor habitats in the Bay of Fundy to assess megafaunal assemblages associated with *Modiolus modiolus* beds. *Estuar. Coast. Shelf Sci.* **2021**, *252*, 107294. <https://doi.org/10.1016/j.ecss.2021.107294>.
- Sutton, G. *Irish Sea Marine Aggregate Initiative (IMAGIN)*; Project Synthesis Report Including: Geological Assessment, Environmental Assessment, Morphodynamic Modelling Web-based GIS System, Cost Benefit Analysis, Aggregate Resources and Markets-Wales, Marine Environment, no. 36.; Marine Institute: St. John’s, NL, Canada, 2008.
- Lewis, M.J.; Neill, S.P.; Elliott, A.J. Interannual variability of two offshore sand banks in a region of extreme tidal range. *J. Coast. Res.* **2015**, *31*, 265–275. <https://doi.org/10.2112/JCOASTRES-D-14-00010.1>.
- Phillips, M.R.; Jones, A.L. Erosion and tourism infrastructure in the coastal zone: Problems, consequences and management. *Tour. Manag.* **2006**, *27*, 517–524. <https://doi.org/10.1016/j.tourman.2005.10.019>.
- Distefano, S.; Gamberi, F. Preservation of Transgressive System Tract Geomorphic Elements during the Holocene Sea Level Rise in the South-Eastern Sicilian Tyrrhenian Margin. *J. Mar. Sci. Eng.* **2022**, *10*, 1013. <https://doi.org/10.3390/jmse10081013>.
- Morelissen, R.; Hulscher, S.J.M.H.; Knaapen, M.A.F.; Németh, A.A.; Bijker, R. Mathematical modelling of sand wave migration and the interaction with pipelines. *Coast. Eng.* **2003**, *48*, 197–209. [https://doi.org/10.1016/S0378-3839\(03\)00028-0](https://doi.org/10.1016/S0378-3839(03)00028-0).

16. Yaghoobi, M.; Mazaheri, S.; Jabbari, E. Determining Natural Frequency of Free Spanning Offshore Pipelines by Considering the Seabed Soil Characteristics. *J. Persian Gulf* **2012**, *3*, 25–34.
17. Sumer, B.M.; Fredsøe, J.; Christiansen, N. Scour around vertical pile in waves. *J. Waterw. Port Coast. Ocean. Eng.* **1992**, *118*, 15–31. [https://doi.org/10.1061/\(ASCE\)0733-950X\(1992\)118:1\(15\)](https://doi.org/10.1061/(ASCE)0733-950X(1992)118:1(15)).
18. Whitehouse, R.J.S.; Harris, J.M.; Sutherland, J.; Rees, J. The nature of scour development and scour protection at offshore wind-farm foundations. *Mar. Pollut. Bull.* **2011**, *62*, 73–88. <https://doi.org/10.1016/j.marpolbul.2010.09.007>.
19. Department of the Environment Climate and Communications. *Climate Action Plan 2021*; Department of the Environment Climate and Communications: Dublin, Ireland, 2021.
20. European Commission. REPowerEU: A plan to rapidly reduce dependence on Russian fossil fuels and fast forward the green transition. *Press Release*, 2022. Available online: https://ec.europa.eu/commission/presscorner/detail/en/IP_22_3131 (accessed on 27 September 2022).
21. National Grid. *ESO Pathway to 2030: A Holistic Network Design to Support Offshore Wind Deployment for Net Zero*; National Grid: Warwick, UK, 2022.
22. Pickering, M.D.; Wells, N.C.; Horsburgh, K.J.; Green, J.A.M. The impact of future sea-level rise on the European Shelf tides. *Cont. Shelf Res.* **2012**, *35*, 1–15. <https://doi.org/10.1016/j.csr.2011.11.011>.
23. Pickering, M.D.; Horsburgh, K.J.; Blundell, J.R.; Hirschi, J.J.M.; Nicholls, R.J.; Verlaan, M.; Wells, N.C. The impact of future sea-level rise on the global tides. *Cont. Shelf Res.* **2017**, *142*, 50–68. <https://doi.org/10.1016/j.csr.2017.02.004>.
24. Stow, D.A.V.; Hernández-Molina, F.J.; Llave, E.; Sayago-Gil, M.; Río, V.D.; Branson, A. Bedform-velocity matrix: The estimation of bottom current velocity from bedform observations. *Geology* **2009**, *37*, 327–330. <https://doi.org/10.1130/G25259A.1>.
25. Dyer, K.R.; Huntley, D.A. The origin, classification and modelling of sand banks and ridges. *Cont. Shelf Res.* **1999**, *19*, 1285–1330. [https://doi.org/10.1016/S0278-4343\(99\)00028-X](https://doi.org/10.1016/S0278-4343(99)00028-X).
26. Holmes, R.; Tappin, D.R. DTI Strategic Environmental Assessment Area 6, Irish Sea, seabed and surficial geology and processes. British Geological Survey Commissioned Report, CR/05/057, p. 82, 2005. Available online: <http://nora.nerc.ac.uk/11259/> (accessed on 16 March 2021).
27. Jackson, D.I.; Jackson, A.A.; Evans, D.J.A.; Wingfield, R.T.R.; Barnes, R.P.; Arthur, M.J. *United Kingdom Offshore Regional Report: The Geology of the Irish Sea*; HMSO for the British Geological Survey: London, UK, 1995.
28. Johnson, M.A.; Kenyon, N.H.; Belderson, R.H.; Stride, A.H. Sand transport. In *Offshore Tidal Sands: Processes and Deposits*; Stride, A.H., Ed.; Chapman and Hall: London, UK, 1982, pp. 58–94. https://doi.org/10.1007/978-94-009-5726-8_4.
29. Knaapen, M.A.F. Sandwave migration predictor based on shape information. *J. Geophys. Res. Earth Surf.* **2005**, *110*, 1–9. <https://doi.org/10.1029/2004JF000195>.
30. van Landeghem, K.J.J.; Baas, J.H.; Mitchell, N.C.; Wilcockson, D.; Wheeler, A.J. Reversed sediment wave migration in the Irish Sea, NW Europe: A reappraisal of the validity of geometry-based predictive modelling and assumptions. *Mar. Geol.* **2012**, *295*, 95–112. <https://doi.org/10.1016/j.margeo.2011.12.004>.
31. Nemeth, A.; Hulscher, S.J.M.H.; de Vriend, H.J. Offshore sand wave dynamics, engineering problems and future solutions. *Pipeline Gas. J.* **2003**, *230*, 67–69.
32. Couldrey, A.J.; Benson, T.; Knaapen, M.A.F.; Marten, K.V.; Whitehouse, R.J.S. Morphological evolution of a barchan dune migrating past an offshore wind farm foundation. *Earth Surf. Process. Landf.* **2020**, *45*, 2884–2896. <https://doi.org/10.1002/esp.4937>.
33. Park, H.; Vincent, C.E. Evolution of Scroby Sands in the East Anglian coast, UK. *J. Coast. Res.* **2007**, 868–873. <http://www.jstor.org/stable/26481705>.
34. Schmitt, T.; Mitchell, N.C.; Ramsay, T.S. Use of swath bathymetry in the investigation of sand dune geometry and migration around a near shore ‘banner’ tidal sandbank. *Geol. Soc. Spec. Publ.* **2007**, *274*, 53–64. <https://doi.org/10.1144/GSL.SP.2007.274.01.07>.
35. Caston, V.N.D. Linear sand banks in the southern North Sea. *Sedimentology* **1972**, *18*, 63–78. <https://doi.org/10.1111/j.1365-3091.1972.tb00003.x>.
36. Kenyon, N.H.; Cooper, B. *Sand Banks, Sand Transport and Offshore Wind Farms: DTI SEA 6 Technical Report*; ABPmer for Department of Trade and Industry: London, UK, 2005.
37. Leenders, S.; Damveld, J.H.; Schouten, J.; Hoekstra, R.; Roetert, T.J.; Borsje, B.W. Numerical modelling of the migration direction of tidal sand waves over sand banks. *Coast. Eng.* **2021**, *163*, 103790. <https://doi.org/10.1016/j.coastaleng.2020.103790>.
38. Horrillo-Caraballo, J.M.; Yin, Y.; Fairley, I.; Karunaratna, H.; Masters, I.; Reeve, D.E. A comprehensive study of the tides around the Welsh coastal waters. *Estuar. Coast. Shelf Sci.* **2021**, *254*, 107326. <https://doi.org/10.1016/j.ecss.2021.107326>.
39. van Landeghem, K.J.J.; Uehara, K.; Wheeler, A.J.; Mitchell, N.C.; Scourse, J.D. Post-glacial sediment dynamics in the Irish Sea and sediment wave morphology: Data-model comparisons. *Cont. Shelf Res.* **2009**, *29*, 1723–1736. <https://doi.org/10.1016/j.csr.2009.05.014>.
40. EMODnet Bathymetry Consortium, EMODnet Digital Bathymetry (DTM 2020), 2020. <https://doi.org/10.12770/bb6a87dd-e579-4036-abe1-e649cea9881a> (accessed on 12 June 2021).
41. EMODnet Geology, Seabed Substrates. 2019. Available online: <https://www.emodnet-geology.eu/data-products/seabed-substrates/> (accessed on 25 June 2021).
42. Cataño-Lopera, Y.A.; García, M.H. Geometry and migration characteristics of bedforms under waves and currents. Part 1: Sand-wave morphodynamics. *Coast. Eng.* **2006**, *53*, 767–780. <https://doi.org/10.1016/j.coastaleng.2006.03.007>.

43. Xu, J.P.; Wong, F.L.; Kvittek, R.; Smith, D.P.; Paull, C.K. Sandwave migration in Monterey Submarine Canyon, Central California. *Mar. Geol.* **2008**, *248*, 193–212. <https://doi.org/10.1016/j.margeo.2007.11.005>.
44. Dobson, M.R.; Evans, W.E.; James, K.H. The sediment on the floor of the southern Irish Sea. *Mar. Geol.* **1971**, *11*, 27–69. [https://doi.org/10.1016/0025-3227\(71\)90083-1](https://doi.org/10.1016/0025-3227(71)90083-1).
45. Damen, J.M.; van Dijk, T.A.G.P.; Hulscher, S.J.M.H. Spatially Varying Environmental Properties Controlling Observed Sand Wave Morphology. *J. Geophys. Res. Earth Surf.* **2018**, *123*, 262–280. <https://doi.org/10.1002/2017JF004322>.
46. Ashley, G.M. Classification of large-scale subaqueous bedforms: A new look at an old problem; SEPM bedforms and bedding structures. *J. Sediment. Petrol.* **1990**, *60*, 160–172. <https://doi.org/10.1306/212f9138-2b24-11d7-8648000102c1865d>.
47. Flemming, B.W. Zur klassifikation subaquatischer, strömungstransversaler Transportkörper. *Boch. Geol. Und. Geotech. Arb.* **1988**, *29*, 93–97.
48. Flemming, B.W. The role of grain size, water depth and flow velocity as scaling factors controlling the size of subaqueous dunes. *Mar. Sandwave Dyn.* **2000**, *154*, 55–60.
49. Kubo, Y.; Soh, W.; Machiyama, H.; Tokuyama, H. Bedforms produced by the Kuroshio Current passing over the northern Izu Ridge. *Geo-Mar. Lett.* **2004**, *24*, 1–7. <https://doi.org/10.1007/s00367-003-0134-1>.
50. Blondeaux, P.; Vittori, G. A parameterization of the wavelength of tidal dunes. *Earth Surf. Process. Landf.* **2011**, *36*, 1152–1161. <https://doi.org/10.1002/esp.2137>.
51. van Santen, R.B.; de Swart, H.E.; van Dijk, T.A.G.P. Sensitivity of tidal sand wavelength to environmental parameters: A combined data analysis and modelling approach. *Cont. Shelf Res.* **2011**, *31*, 966–978. <https://doi.org/10.1016/j.csr.2011.03.003>.
52. Yalin, M.S. Geometrical properties of sand wave. *J. Hydraul. Div.* **1964**, *90*, 105–119.
53. van der Veen, H.H.; Hulscher, S.J.M.H.; Knaapen, M.A.F. Grain size dependency in the occurrence of sand waves. *Ocean. Dyn.* **2006**, *56*, 228–234. <https://doi.org/10.1007/s10236-005-0049-7>.
54. Franzetti, M.; le Roy, P.; Delacourt, C.; Garlan, T.; Cancouët, R.; Sukhovich, A.; Deschamps, A. Giant dune morphologies and dynamics in a deep continental shelf environment: Example of the banc du four (Western Brittany, France). *Mar. Geol.* **2013**, *346*, 17–30. <https://doi.org/10.1016/j.margeo.2013.07.014>.
55. Bartholdy, J.; Bartholomae, A.; Flemming, B.W. Grain-size control of large compound flow-transverse bedforms in a tidal inlet of the Danish Wadden Sea. *Mar. Geol.* **2002**, *188*, 391–413. [https://doi.org/10.1016/S0025-3227\(02\)00419-X](https://doi.org/10.1016/S0025-3227(02)00419-X).
56. van Landeghem, K.J.J.; Wheeler, A.J.; Mitchell, N.C.; Sutton, G. Variations in sediment wave dimensions across the tidally dominated Irish Sea, NW Europe. *Mar. Geol.* **2009**, *263*, 108–119. <https://doi.org/10.1016/j.margeo.2009.04.003>.
57. Hulscher, S.J.M.H. Tidal-induced large-scale regular bed form patterns in a three-dimensional shallow water model. *J. Geophys. Res. Ocean.* **1996**, *101*, 20727–20744. <https://doi.org/10.1029/96JC01662>.
58. Blondeaux, P.; Vittori, G. Formation of tidal sand waves: Effects of the spring-neap cycle. *J. Geophys. Res. Ocean.* **2010**, *115*, 1–7. <https://doi.org/10.1029/2010JC006400>.
59. Campmans, G.H.P.; Roos, P.C.; de Vriend, H.J.; Hulscher, S.J.M.H. The Influence of Storms on Sand Wave Evolution: A Non-linear Idealized Modeling Approach. *J. Geophys. Res. Earth Surf.* **2018**, *123*, 2070–2086. <https://doi.org/10.1029/2018JF004616>.
60. Borsje, B.W.; Kranenburg, W.M.; Roos, P.C.; Matthieu, J.; Hulscher, S.J.M.H. The role of suspended load transport in the occurrence of tidal sand waves. *J. Geophys. Res. Earth Surf.* **2014**, *119*, 701–716. <https://doi.org/10.1002/2013JF002828>.
61. Ernsten, V.B.; Noormets, R.; Winter, C.; Hebbeln, D.; Bartholomä, A.; Flemming, B.W.; Bartholdy, J. Development of subaqueous barchanoid-shaped dunes due to lateral grain size variability in a tidal inlet channel of the Danish Wadden Sea. *J. Geophys. Res. Earth Surf.* **2005**, *110*, 1–13. <https://doi.org/10.1029/2004JF000180>.
62. Francken, F.; Stanislas, W.; Parker, R.; Taverniers, E. Factors influencing subaqueous dunes in the Scheldt Estuary. *Geo-Mar. Lett.* **2004**, *24*, 14–21. <https://doi.org/10.1007/s00367-003-0154-x>.
63. Dalrymple, R.W.; Knight, R.J.; Lambiase, J.J. Bedforms and their hydraulic stability relationships in a tidal environment, Bay of Fundy, Canada. *Nature* **1978**, *275*, 100–104. <https://doi.org/10.1038/275100a0>.
64. Coughlan, M.; Guerrini, M.; Creane, S.; O’Shea, M.; Ward, S.L.; van Landeghem, K.J.J.; Murphy, J.; Doherty, P. A new seabed mobility index for the Irish Sea: Modelling seabed shear stress and classifying sediment mobilisation to help predict erosion, deposition, and sediment distribution. *Cont. Shelf Res.* **2021**, *229*, 104574. <https://doi.org/10.1016/j.csr.2021.104574>.
65. Tappin, D.R.; Chadwick, R.A.; Jackson, A.A.; Wingfield, R.T.R.; Smith, N.J.P. *United Kingdom Offshore Regional Report: The Geology of Cardigan Bay and the Bristol Channel*; HMSO for the British Geological Survey: London, UK, 1994.
66. Wheeler, A.J.; Walshe, J.; Sutton, G.D. Geological appraisal of the Kish, Burford, Bray and Fraser Banks, Outer Dublin Bay Area. In *Marine Resources Series*; Marine Institute: Dublin, Ireland, 2000.
67. Kozachenko, M.; Fletcher, R.; Sutton, G.; Monteys, X.; van Landeghem, K.; Wheeler, A.; Lassoued, Y.; Cooper, A.; Nicoll, C. *A Geological Appraisal of Marine Aggregate Resources in the Southern Irish Sea*; Technical report produced for the Irish Sea Marine Aggregates Initiative (IMAGIN) project funded under the INTERREG IIIA Community Initiative Programme 2000–2006; University College Cork, Ireland, 2008.
68. Ward, S.L.; Neill, S.P.; van Landeghem, K.J.J.; Scourse, J.D. Classifying seabed sediment type using simulated tidal-induced bed shear stress. *Mar. Geol.* **2015**, *367*, 94–104. <https://doi.org/10.1016/j.margeo.2015.05.010>.
69. Coughlan, M.; Long, M.; Doherty, P. Geological and geotechnical constraints in the Irish Sea for offshore renewable energy. *J. Maps* **2020**, *16*, 420–431. <https://doi.org/10.1080/17445647.2020.1758811>.
70. Hanna, J.E.; Cooper, J.A.G. Mesoscale Morphological Changes on Linear, Nearshore Sandbanks, Co. Wexford, SE Ireland. *J. Coast. Res.* **2002**, *36*, 356–364. <https://doi.org/10.2112/1551-5036-36.sp1.356>.

71. Panigrahi, J.K.; Ananth, P.N.; Umesh, P.A. Coastal morphological modeling to assess the dynamics of Arklow Bank, Ireland. *Int. J. Sediment. Res.* **2009**, *24*, 299–314. [https://doi.org/10.1016/S1001-6279\(10\)60005-4](https://doi.org/10.1016/S1001-6279(10)60005-4).
72. Walbridge, S.; Slocum, N.; Pobuda, M.; Wright, D.J. Unified Geomorphological Analysis Workflows with Benthic Terrain Modeler. *Geosciences* **2018**, *8*. <https://doi.org/10.3390/GEOSCIENCES8030094>.
73. Jasiewicz, J.; Stepinski, T.F. Geomorphons—a pattern recognition approach to classification and mapping of landforms. *Geomorphology* **2013**, *182*, 147–156. <https://doi.org/10.1016/j.geomorph.2012.11.005>.
74. Summers, G.; Lim, A.; Wheeler, A.J. A scalable, supervised classification of seabed sediment waves using an object-based image analysis approach. *Remote Sens.* **2021**, *13*, 1–29. <https://doi.org/10.3390/rs13122317>.
75. van Dijk, T.A.G.P.; Lindenberg, R.C.; Egberts, P.J.P. Separating bathymetric data representing multiscale rhythmic bed forms: A geostatistical and spectral method compared. *J. Geophys. Res. Earth Surf.* **2008**, *113*, 1–16. <https://doi.org/10.1029/2007JF000950>.
76. Duffy, G.P. Patterns of morphometric parameters in a large bedform field: Development and application of a tool for automated bedform morphometry. *Ir. J. Earth Sci.* **2012**, *30*, 31–39. <https://doi.org/10.3318/IJES.2012.30.31>.
77. van der Mark, C.F.; Blom, A. *A New and Widely Applicable Tool for Determining the Geometric Properties of Bedforms*. Report number: CE&M Research Report 2007R-003/WEM-002, University of Twente, Faculty of Engineering Technology, The Netherlands, 2007. <https://doi.org/10.13140/RG.2.2.17637.40161>.
78. Wang, L.; Yu, Q.; Zhang, Y.; Flemming, B.W.; Wang, Y.; Gao, S. An automated procedure to calculate the morphological parameters of superimposed rhythmic bedforms. *Earth Surf. Process. Landf.* **2020**, *45*, 3496–3509. <https://doi.org/10.1002/esp.4983>.
79. Evans, W.; Benetti, S.; Sacchetti, F.; Jackson, D.W.T.; Dunlop, P.; Monteys, X. Bedforms on the northwest Irish Shelf: Indication of modern active sediment transport and overprinting of paleo-glacial sedimentary deposits. *J. Maps* **2015**, *11*, 561–574. <https://doi.org/10.1080/17445647.2014.956820>.
80. Berne, S.; Castaing, P.; le Drezen, E.; Lericolais, G. Morphology, internal structure, and reversal of asymmetry of large subtidal dunes in the entrance to Gironde Estuary (France). *J. Sediment. Petrol.* **1993**, *63*, 780–793. <https://doi.org/10.1306/d4267c03-2b26-11d7-8648000102c1865d>.
81. di Stefano, M.; Mayer, L.A. An automatic procedure for the quantitative characterization of submarine bedforms. *Geosciences* **2018**, *8*, 1–26. <https://doi.org/10.3390/geosciences8010028>.
82. Dove, D.; Bradwell, T.; Carter, G.; Cotterill, C.; Gafeira Goncalves, J.; Green, S.; Krabbendam, M.; Mellett, C.; Stevenson, A.; Stewart, H.; et al. *Seabed Geomorphology: A Two-Part Classification System*. Marine Geoscience Programme. Open Report OR/16/001; British Geological Survey: Nottingham, UK, 2016.
83. Kaklamanos, J.; Elmy, K. *geotech: Geotechnical Engineering. R package version 1.0, R: A language and environment for statistical computing*, <http://www.r-project.org/>, 2016.
84. DHI Group *MIKE 21 Toolbox: User guide*; DHI Group: Brisbane, QLD, Australia, 2017.
85. DHI Group *MIKE 21 Flow Model: Hydrodynamic Module User Guide*; DHI Group: Brisbane, QLD, Australia, 2017.
86. Shields, A. Anwendung der Aehnlichkeitsmechanik und der Turbulenzforschung auf die Geschiebebewegung. Preussischen Versuchsanstalt für Wasserbau. Ph.D. Thesis, Technical University Berlin, Berlin, Germany, 1936.
87. Evans, J. D. *Straightforward Statistics for the Behavioral Sciences*; Brooks/Cole Publishing: Pacific Grove, CA, 1996.
88. Huthnance, J.M. On one mechanism forming linear sand banks. *Estuar. Coast. Shelf Sci.* **1982**, *14*, 79–99. [https://doi.org/10.1016/S0302-3524\(82\)80068-6](https://doi.org/10.1016/S0302-3524(82)80068-6).
89. Hulscher, S.J.M.H.; de Swart, H.E.; de Vriend, H.J. The generation of offshore tidal sand banks and sand waves. *Cont. Shelf Res.* **1993**, *13*, 1183–1204. [https://doi.org/10.1016/0278-4343\(93\)90048-3](https://doi.org/10.1016/0278-4343(93)90048-3).
90. Fairley, I.; Masters, I.; Karunaratna, H. Numerical modelling of storm and surge events on offshore sandbank. *Mar. Geol.* **2016**, *371*, 106–119. <https://doi.org/10.1016/j.margeo.2015.11.007>.
91. McCarroll, R.J.; Masselink, G.; Valiente, N.G.; Wiggins, M.; Scott, T.; Conley, D.C.; King, E.V. Impact of a headland-associated sandbank on shoreline dynamics. *Geomorphology* **2020**, *355*, 107065. <https://doi.org/10.1016/j.geomorph.2020.107065>.
92. Pingree, R.D. The formation of the Shambles and other banks by tidal stirring of the sea. *J. Mar. Biol. Assoc. United Kingd.* **1978**, *58*, 211–226. <https://doi.org/10.1017/S0025315400024504>.
93. Bastos, A.; Collins, M.; Kenyon, N. Water and sediment movement around a coastal headland: Portland Bill, southern UK. *Ocean. Dyn.* **2003**, *53*, 309–321. <https://doi.org/10.1007/s10236-003-0031-1>.
94. Berthot, A.; Pattiaratchi, C. Mechanisms for the formation of headland-associated linear sandbanks. *Cont. Shelf Res.* **2006**, *26*, 987–1004. <https://doi.org/10.1016/j.csr.2006.03.004>.
95. Li, M.Z.; Shaw, J.; Todd, B.J.; Kostylev, V.E.; Wu, Y. Sediment transport and development of banner banks and sandwaves in an extreme tidal system: Upper Bay of Fundy, Canada. *Cont. Shelf Res.* **2014**, *83*, 86–107. <https://doi.org/10.1016/j.csr.2013.08.007>.
96. Wentworth, C.K. A Scale of Grade and Class Terms for Clastic Sediments. *J. Geol.* **1922**, *30*, 377–392. <https://doi.org/10.1086/622910>.
97. Neill, S.P.; Couch, S.J. Impact of Tidal Energy Converter (TEC) Array Operation on Sediment Dynamics. In Proceedings of the 9th European Wave and Tidal Energy Conference (EWTEC), Southampton, UK, 5–9 September 2011.
98. Uehara, K.; Scourse, J.D.; Horsburgh, K.J.; Lambek, K.; Purcell, A.P. Tidal evolution of the northwest European shelf seas from the Last Glacial Maximum to the present. *J. Geophys. Res. Ocean.* **2006**, *111*, 1–15. <https://doi.org/10.1029/2006JC003531>.
99. O’Shea, M.P. Monitoring and modelling the morphodynamic evolution of a breached barrier beach system,” University College Cork, 2015. Available online: <https://cora.ucc.ie/handle/10468/3359> (accessed on 15 May 2021).

100. Colosimo, I.; de Vet, P.L.M.; van Maren, D.S.; Reniers, A.J.H.M.; Winterwerp, J.C.; van Prooijen, B.C. The impact of wind on flow and sediment transport over intertidal flats. *J. Mar. Sci. Eng.* **2020**, *8*, 1–26. <https://doi.org/10.3390/jmse8110910>.
101. Daniell, J.J. Bedload parting in western Torres Strait, northern Australia. *Cont. Shelf Res.* **2015**, *93*, 58–69. <https://doi.org/10.1016/j.csr.2014.11.008>.
102. Giardino, A.; Monbaliu, J. Wave effects on the morphodynamic evolution of an offshore sand bank. *J. Coast. Res. SI* **2010**, *51*, 127–140. <https://doi.org/10.2112/SI51-012.1>.
103. Idier, D.; Ehrhold, A.; Garlan, T. Morphodynamique d'une dune sous-marine du détroit du pas de Calais. *Comptes. Rendus Geosci.* **2002**, *334*, 1079–1085. [https://doi.org/10.1016/s1631-0713\(02\)01852-7](https://doi.org/10.1016/s1631-0713(02)01852-7).
104. Mitchell, N.C.; Jerrett, R.; Langman, R. Dynamics and stratigraphy of a tidal sand ridge in the Bristol Channel (Nash Sands banner bank) from repeated high-resolution multibeam echo-sounder surveys. *Sedimentology* **2022**, *69*, 1051–1082. <https://doi.org/10.1111/sed.12935>.
105. van Dijk, T.A.G.P.; Kleinhans, M.G. Processes controlling the dynamics of compound sand waves in the North Sea, Netherlands. *J. Geophys. Res. Earth Surf.* **2005**, *110*, 1–15. <https://doi.org/10.1029/2004JF000173>.